ABSTRACT

Title of Thesis: QUANTITATIVE UNDERSTANDING OF TEMPERATURE RISE AND SAFETY IN HIGH–ENERGY SOLID–STATE BATTERIES.

TAIWO OLADAPO OGUNDIPE, MASTER OF SCIENCE, 2024.

Thesis Directed By: DR. PAUL ALBERTUS, DEPARTMENT OF CHEMICAL AND BIOMOLECULAR ENGINEERING.

The rising demand for renewable energy and electric transportation has increased the need for advanced and safer battery technologies. Conventional lithium – ion batteries face limitations in energy density and safety risks due to the reaction of oxygen from the decomposed cathodes with other battery components, which can cause thermal runaway, leading to fires or explosions. Solid – state batteries, which use a solid electrolyte, offer a promising solution by potentially improving both energy density and safety. This study focuses on the thermal behavior and heat generation of anode – cathode – electrolyte (ACE) (Li / LPSCl / NMC811) solid-state batteries using differential scanning calorimetry (DSC). The results show significant heat generation, ranging from 4000 to 5400 J/g $_{NMC811}$, with a corresponding adiabatic temperature rise of 1300 – 1750 °C. When small amounts of liquid electrolyte are added, the onset temperature is lowered, and the heat release shifts to higher temperatures. However, the total heat generation remains within a similar range. These findings provide insights into the thermal stability of all – solid –

state batteries , and solid – state batteries with small amount of liquid electrolyte, contributing to the development of safer and higher energy density energy storage systems.

QUANTITATIVE UNDERSTANDING OF TEMPERATURE RISE AND SAFETY IN HIGH – ENERGY SOLID – STATE BATTERIES.

by

Taiwo Oladapo Ogundipe

Thesis submitted to the Faculty of the Graduate School of the
University of Maryland, College Park, in partial fulfillment
of the requirements for the degree of
Master of Science
[2024]

Advisory Committee:
Professor Paul Albertus, Chair
Professor Peter Kofinas
Professor Chunsheng Wang

Acknowledgements

I would like to express my deepest gratitude to my advisor, Dr. Paul Albertus, for his invaluable guidance, (financial) support, and mentorship throughout this research journey. His deep knowledge and insightful feedback have been instrumental in shaping my work, and I am grateful for the opportunities he has provided me to grow both academically and professionally.

A special thanks goes to Bhuvsmita Bhargava, Zixuan Wang, and Karl Larson, whose contributions to various aspects of this research were immensely helpful. Your collaboration, technical support, and insights made a significant difference, and I truly appreciate your efforts. I am also deeply thankful to all my colleagues and lab members for their support and assistance during this research. Working alongside such talented and supportive individuals was a privilege, and your willingness to offer advice, troubleshoot challenges, and share knowledge has been a constant source of encouragement. To my family and friends, your unwavering support and understanding have been a source of strength and motivation. Thank you for believing in me and encouraging me throughout this journey.

Lastly, I am grateful to Ford, the Center for Research in Extreme Batteries (CREB), and the University of Maryland College Park for the resources, funding, and state – of – the – art laboratory facilities that made this research possible. This work would not have been accomplished without the technical infrastructure and support provided. This

thesis is the result of a collective effort, and I am deeply thankful to everyone who played a role in its completion.

Table of Contents

Acknowledgements ii
Table of Contents iv
List of Tables vi
List of Figures vii
List of Abbreviations viii
Chapter 1: Introduction 1
1.1. Background on Solid – state Battery Safety 1
1.1.1. NMC Cathode Materials 3
1.1.2. Argyrodite solid electrolyte 5
1.1.3. High – capacity Anodes 6
1.2. Introduction to Differential Scanning Calorimetry (DSC) Measurements 7
1.3. Literature Review 8
1.4. Thesis Focus 10
Chapter 2: Methodology 12
2.1. Materials Preparation 12
2.2. Split Cell Preparation 13
2.3. Anode – Cathode – Electrolyte (ACE) Sample Preparation 13
2.4. Differential Scanning Calorimetry Measurements 14
2.5. Method of Integration 15
Chapter 3: Results and Discussion 17
3.1. Component DSC Results 17
3.1.1. $Li_{0.2}$NMC811 cathode sheet 17
3.1.2. LPSCl Shard 17
3.1.3. $Li_{0.2}$NMC811 cathode sheet + LPSCl Shard 19
3.1.4. Liquid electrolyte ($LiPF_6$ in EC: DEC: 1:1 v/v) 19
3.1.5. $Li_{0.2}$NMC811 cathode sheet + Liquid Electrolyte 22
3.1.6. Li metal 23
3.1.7. Li metal + LPSCl Shard 23
3.2. ACE Sample DSC Results 24
3.2.1. ACE Sample (NMC811 + Hot – pressed LPSCl + Li metal) 24
3.2.2. ACE Sample (NMC811 + Cold – pressed LPSCl + Li metal) 26
3.3. Effect of Liquid Electrolyte on the Heat Generation 27
Chapter 4: Conclusion 31
4.1. Results Summary 31
4.2. Limitations to Current Work 32
4.3. Recommendations and Future Work 33
Appendices 34
A.1*:* Sample MATLAB Algorithms for fitting and integrating raw DSC heat flow data 34
A.2*:* DSC heat flow of LPSCl shard. Reproduced from [24] 38
A.3: DSC heat flow of 1M $LiPF_6$ in EC:DEC (1:1 v/v). Reproduced from Roth *et al*.[25] 39

A.4: DSC heat flow of 1M $LiPF_6$ in EC:DEC (1:1 v/v). Reproduced from Wang *et al.*[26] 39
A.5: Calculations to determine the maximum volume of liquid electrolyte used in ACE samples 40
Bibliography 42

List of Tables

Table 1: Comparison of the onset temperature, heat release, and adiabatic temperature rise of different battery chemistries ……..30

List of Figures

Figure 1.1: Conventional Lithium – ion Battery …….. 2
Figure 1.2: Mass spectrometry profiles of different NMC cathodes with varying nickel contents ……. 4
Figure 1.3: Challenges of nickel rich – NMC cathode materials ……. 4
Figure 1.4: Challenges and improvement strategies of lithium metal anode material ……. 7
Figure 1.5: Schematic diagram of a differential scanning calorimetry …… 8
Figure 1.6: Thermal stability and optical images of the solid-state pouch cell at 0% and 100% SOC …… 9
Figure 1.7: An overview of my research …… 11
Figure 2.1: Li_6PS_5Cl sulfide solid electrolyte pellet (0.870 mm thick and 0.5 – inch diameter) ……. 12
Figure 2.2: ACE Sample Setup ……...……... 15
Figure 2.3: (a). Variations in the raw empty pan baselines. (b). Raw heat flow and the Baseline – corrected heat flow …… 16
Figure 3.1: Raw DSC result of $Li0.2$NMC811 cathode sheet ……. 18
Figure 3.2: Raw DSC result of LPSCl shard …….. 18
Figure 3.3: (a) Baseline – corrected DSC result of $Li_{0.2}$NMC811 cathode sheet + LPSCl Shard. (b) Comparison with $Li_{0.2}$NMC811 cathode sheet only. (c) Integrated area of $Li_{0.2}$NMC811 cathode sheet + LPSCl Shard ……... 20
Figure 3.4: (a) Baseline – corrected DSC result of the liquid electrolyte. (b) Integrated DSC result of the liquid electrolyte ……. 21
Figure 3.5: (a). Raw DSC result of the $Li_{0.2}$NMC811 cathode sheet with liquid electrolyte. (b) Raw DSC result of the comparison of $Li_{0.2}$NMC811 sheets with ($Li_{0.2}$NMC811 sheets + liquid electrolyte) …….. 22
Figure 3.6. Raw DSC result of the Li metal ……... 23
Figure 3.7: Raw DSC result of the reaction of lithium with LPSCl shard ……. 24
Figure 3.8: (a) Baseline – corrected DSC result of the ACE sample with hot – pressed LPSCl shard. (b) Cumulative heat flow of the ACE sample ……... 25
Figure 3.9: (a). Baseline – corrected DSC result of the ACE sample with hot – pressed LPSCl shard. (b). Cumulative heat flow of the ACE sample …….. 26
Figure 3.10: Baseline – corrected DSC result of the ACE sample with varying amounts of liquid electrolyte ……..... 27
Figure 3.11: Raw DSC result of the ACE sample (a) without and (b) with 0.5 µL liquid electrolyte ……..……. 28

List of Abbreviations

ACE – Anode – Cathode – Electrolyte
ARC – Accelerated Rate Calorimetry
ASSB – All – Solid – State – Battery
CC – Constant Current
CV – Constant Voltage
DEC – Diethyl Carbonate
DSC – Differential Scanning Calorimetry
EC – Ethyl Carbonate
EV – Electric Vehicle
LE – Liquid Electrolyte
LiBs – Lithium-ion Batteries
LPSCl – Lithium Thiophosphate (Li_6PS_5Cl)
MS – Mass Spectrometry
NMC – Nickel Manganese Cobalt Oxide ($LiNi_xMn_yCo_{1-x-y}O_2$)
PVDF – Polyvinylidene Fluoride
SE – Solid Electrolyte
SSE – Solid – State Electrolyte
TGA – Thermal Gravimetric Analysis
XRD – X – ray Diffraction
XPS – X – ray Spectrometry

Chapter 1: Introduction

1.1. Background on Solid – state Battery Safety.

Lithium-ion batteries (LIBs) have emerged as one of the most extensively used energy storage systems, playing a crucial role in powering various technologies ranging from personal electronics like cellphones and laptops to large – scale applications, such as electric vehicles (EVs) and grid storage.[1] (Note: all acronyms are defined in the List of Abbreviations above). The basic structure of a conventional lithium – ion battery consists of an anode typically made of graphite, a cathode composed of lithium metal oxides, a separator, and a liquid organic electrolyte containing lithium salt that facilitates the movement of lithium ions between the electrodes during charge and discharge cycles,[2] as shown in Figure 1.1. As the world increasingly shifts towards renewable energy sources and electric transportation to mitigate the effects of climate change, the demand for advanced battery technologies has surged dramatically. It is projected that global battery demand will continue to rise exponentially in the coming decades, primarily due to the increased adoption of EVs and the need for large – scale energy storage solutions.[3] However, despite their widespread use, conventional lithium – ion batteries have limited energy density (the amount of energy stored per unit volume or mass). Moreover, they pose safety concerns as the liquid electrolytes are flammable and prone to leakage.[4] Battery safety is important to prevent the release of gases within the cell as a result of overcharging, damage, or overheating, which can lead to combustion, rupture, or thermal runaway where the temperatures exceed 500°C. To address these challenges, current research is focused on developing new battery

materials that offer higher energy densities to deliver longer ranges and improved safety.

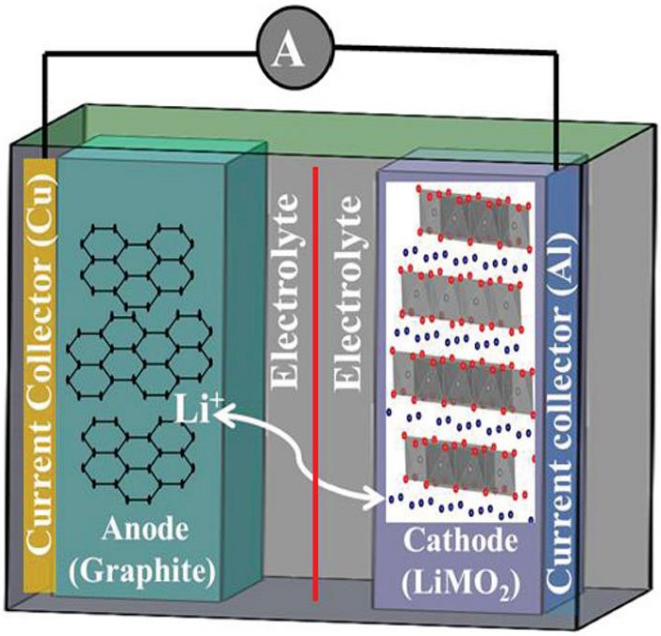

Figure 1.1: Conventional Lithium-ion Battery. Reproduced from [2].

More research is also focused on developing high energy density cathode materials and high – capacity anode materials which can store more energy. Solid – state batteries, which replace the liquid electrolyte in conventional Li – ion batteries with a solid electrolyte, are seen as a good alternative as the solid electrolyte is assumed to address many of the safety concerns associated with liquid electrolytes, reducing the risk of thermal runaway and improving the safety of the battery. However, solid – state batteries still show substantial safety challenges. While solid state batteries offer increased energy density, the high – capacity cathodes are more prone to thermal instability, posing a higher risk of heat generation during thermal runaway.[5]

1.1.1. NMC Cathode Materials.

Lithium nickel manganese cobalt oxide, $LiNi_xMn_yCo_{1-x-y}O_2$ (NMC), is recognized as a highly promising cathode material for next – generation batteries, offering a high specific capacity of approximately 200 mAh g^{-1} and a moderately high average discharge potential of around 3.8 V vs Li^+ / Li. Among these, Ni – rich NMC cathodes ($x > 0.5$), especially $LiNi_{0.8}Mn_{0.1}Co_{0.1}O_2$ (NMC811), are attractive for their increased energy density due to higher nickel content. However, the increased nickel content also increased the reactivity of the cathodes due to the instability of nickel ions at higher temperatures, triggering oxygen release that causes exothermic reactions and making it thermally unstable.[6] Bak *et al* investigated the thermal stability of NMC cathode materials with varying nickel contents using Time – Resolved X-ray diffraction (TR – XRD) and mass spectrometry (MS) up to 600 °C. The results showed that thermal stability of the NMC sheets decreases with increasing nickel content. Specifically, NMC811, which has the highest nickel content among the tested NMC samples, shows the lowest onset temperature for phase transitions and a sharper peak in oxygen release compared to NMC materials with lower nickel content due to the instability of nickel as it undergoes a rapid reduction from Ni^{4+} to Ni^{2+} during thermal decomposition,[7] as shown in Figure 1.2. Furthermore, the effect of varying Ni contents on the electrochemical properties and thermal stability of NMC cathode sheets was studied. It was found that increasing nickel content led to a reduction in the thermal stability and capacity retention of the NMC materials.[8] Also, Ni – rich NMCs exhibit poorer chemical stability under ambient conditions, and experience side reactions with the electrolyte at high voltages.[9] At about 170 °C, the NMC cathode materials start to

decompose and release oxygen, which reacts with electrolyte, resulting in exothermic reactions and potential thermal runaway of LIBs[10] (Figure 1.3).

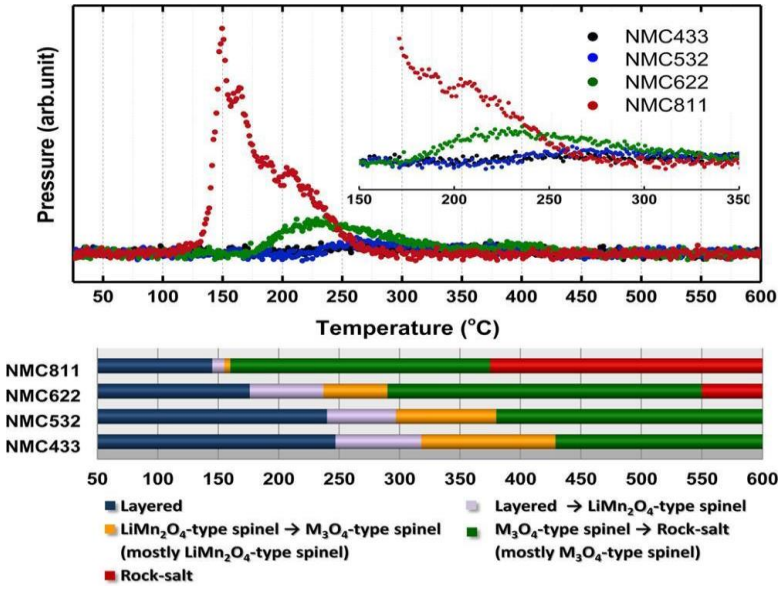

Figure 1.2: Mass spectrometry profiles of different NMC cathodes with varying nickel contents. Reproduced from [7].

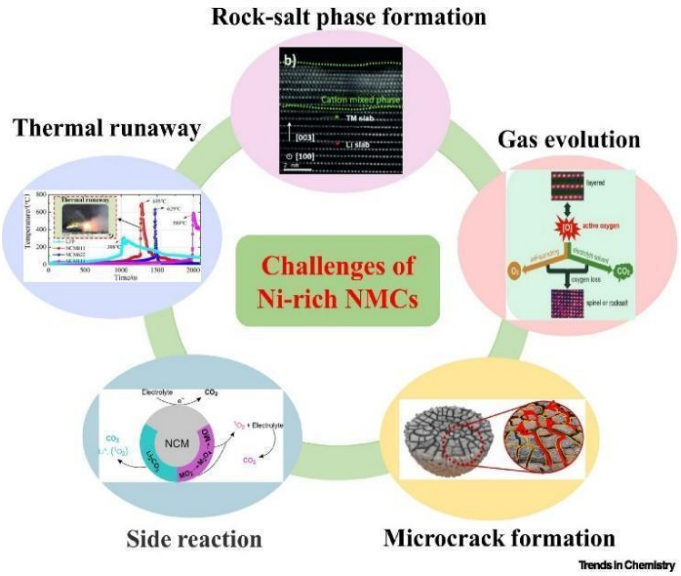

Figure 1.3: Challenges of nickel rich – NMC cathode materials. Reproduced from [9].

1.1.2. Argyrodite solid electrolyte.

Liquid electrolytes (LEs) used in traditional LIBs are flammable, which pose safety issues and limit the operation temperature range of LIBs. These limitations necessitate the development of safer alternatives, leading to the adoption of solid electrolytes, which offer potentially enhanced safety and performance. Recent research has increasingly focused on inorganic solid electrolytes, including sulfides, hydrides, oxides, nitrides, and phosphates. Among these, sulfide – based solid electrolytes have attracted significant attention due to their exceptional ionic conductivity, often surpassing 10^{-3} S / cm at room temperature, distinguishing them from other types of solid electrolyte.[11] One of the key advantages of sulfide solid-state electrolytes (SSEs) is their lower Young's modulus, which results in reduced stress formation and minimized contact loss during volume changes in cell operation. However, sulfide SSEs generally have lower chemical stability compared to oxides and are highly sensitive to atmospheric conditions, leading to a rapid decline in ionic conductivity when exposed to air. As a result, sulfide electrolytes are typically handled in inert – gas – filled gloveboxes to prevent degradation.[12] Among the types of solid electrolytes, argyrodites have emerged as a promising class due to their high ionic conductivity at room temperature, low cost and good compatibility towards lithium metal.[13] Argyrodite – structured sulfide solid electrolytes, such as Li_6PS_5X (X = Cl, Br), have become the dominant choice for all – solid – state battery fabrication due to their exceptional lithium – ion conductivities, reaching up to 2.4 $mS \cdot cm^{-1}$ at room temperature,[13] making them among the most promising solid-state electrolytes for next-generation solid-state batteries.[14]

1.1.3. High – capacity Anodes.

High – capacity anode materials are crucial for advancing lithium – ion batteries, especially as demand for high – performance batteries grow for electric vehicles (EVs) and portable electronics. Traditional Li – ion batteries use graphite as the anode material due to its stable electrochemical performance, but the theoretical specific capacity of the graphite anode material (372 mAh/g) limits its potential for Li – ion batteries.[15] Unlike graphite which store lithium ions within its structure, lithium metal anode uses lithium in its metallic form with a theoretical specific capacity of 3860 mAh/g and an ultra – low redox potential of – 3.04 V versus the standard hydrogen electrode, making it a highly promising anode material for achieving extremely high energy density batteries.[16] However, one of the major problems with Li anode is that it forms dendrites (needle – like lithium deposits that can grow during charging cycles), and penetrates the separator between the anode and cathode, causing short circuits and potentially leading to thermal runaway[17] (Figure 1.4).

Silicon is another promising high – capacity anode material used for batteries due to its extraordinary theoretical capacity of about 4200 mAh/g, which is more than ten times that of conventional graphite anodes.[18] This significant capacity could dramatically increase the energy density of Li – ion batteries, enabling longer driving ranges for EVs, extended battery life for electronic devices, and more efficient energy storage solutions. However, silicon causes large volume expansion during lithiation, causing the silicon particles to fracture, and leading to rapid capacity degradation over repeated charge – discharge cycles.[19]

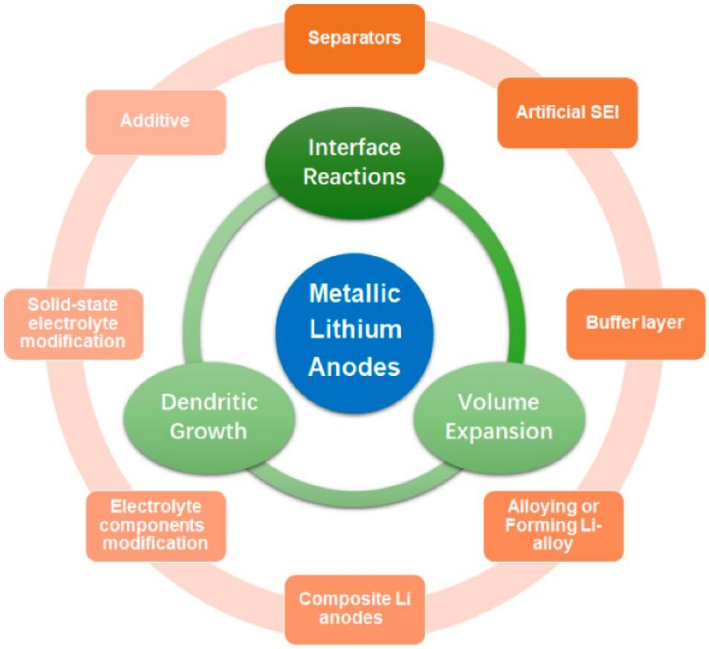

Figure 1.4: Challenges and improvement strategies of lithium metal anode material. Reproduced from [20].

1.2. Introduction to Differential Scanning Calorimetry (DSC) Measurements.

Differential Scanning Calorimetry (DSC) is a widely utilized thermal analysis technique that provides valuable insights into thermal transitions (endothermic or exothermic), including solid – solid and solid – liquid transitions of the components of a cell. By measuring the heat absorbed or released by a material as a function of temperature or time, DSC allows for the precise characterization of thermal properties and behaviors in different materials.[21] In our heat flux DSC setup, the analysis takes place within a chamber containing two pans isolated from the surrounding environment. One pan holds the sample to be analyzed, while the other pan remains

empty and serves as a reference. Both pans are placed on top of two areal thermocouples to measure the temperature changes on both pans, and heated in the chamber through a gas flow stream. As the temperature changes at a constant rate, heat is transferred to the sample and reference, as shown in Figure 1.5, and the heat flow is calculated from the temperature difference between the two pans.[22] The DSC analysis can give valuable information such as the total heat released, onset temperature, and the thermal transitions of the sample in the DSC pans.

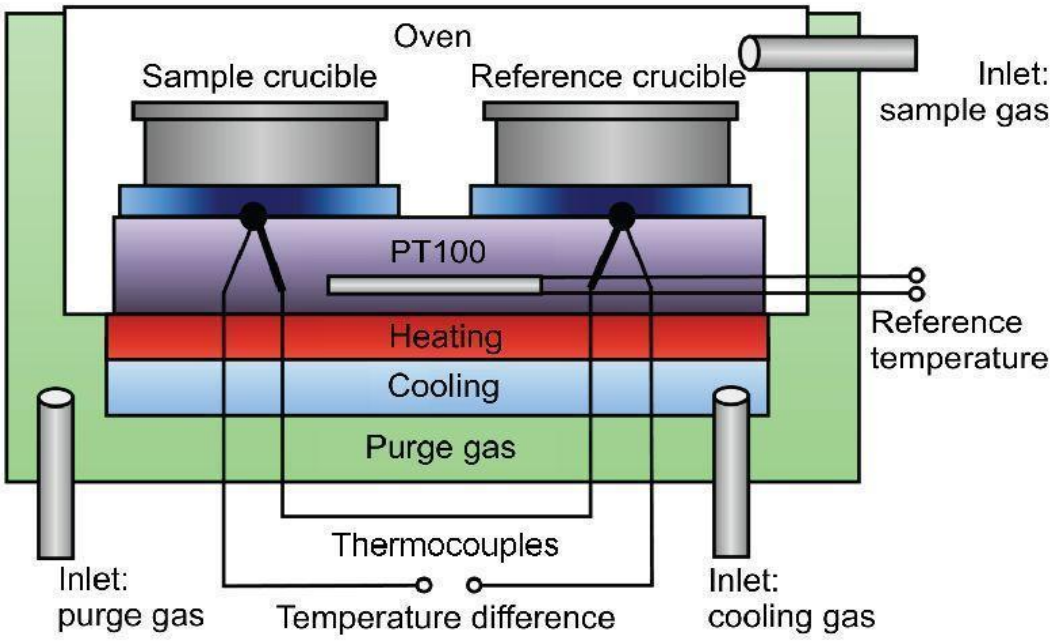

Figure 1.5: Schematic diagram of a differential scanning calorimetry. Reproduced from [22].

1.3. Literature Review.

Few studies have been conducted to investigate the thermal runaway of solid – state batteries. Yang *et al* investigated the thermal stability and oxygen – induced thermal runaway mechanisms in a 3.8 Ah pouch cell comprising lithium metal anode, a

Li_6PS_5Cl solid-state electrolyte, and $LiNi_{0.5}Mn_{0.3}Co_{0.2}O_2$ (NMC532) cathode, using extended-volume accelerating rate calorimetry at 0% and 100% state – of – charge (SOC). At 0% SOC, the cells exhibit high thermal stability, showing only slight self-heating without thermal runaway, due to the formation of a passivating LiCl layer, which results from the mild reaction between lithium metal and the Li_6PS_5Cl electrolyte, limiting further reactions. However, at 100% SOC, thermal runaway occurs at temperatures above 275°C due to the reaction between oxygen released by the decomposing cathode and the solid – state electrolyte (Figure 1.6), while the lithium metal anode itself plays a secondary role, reacting only after the initial runaway is triggered.[23]

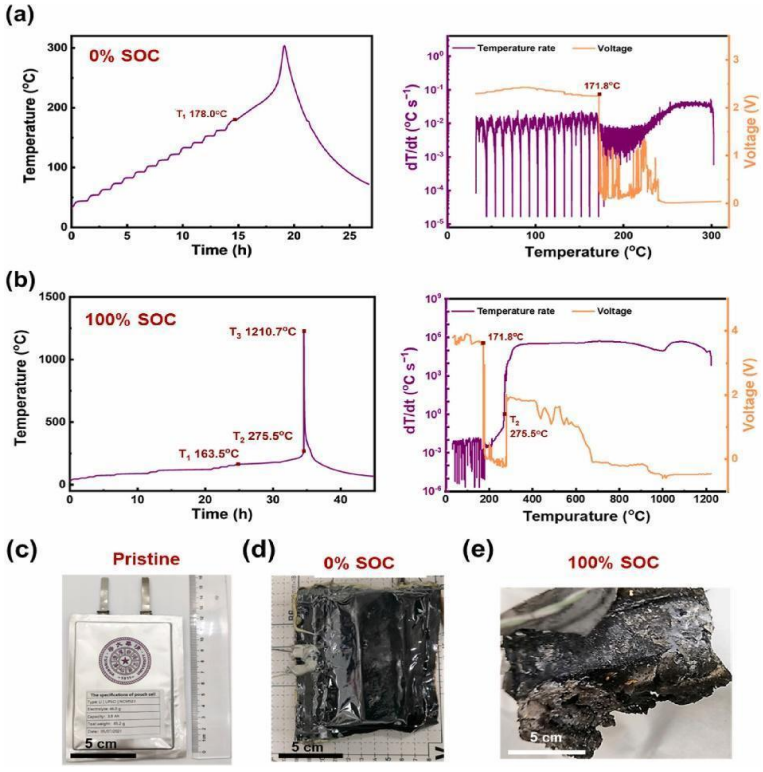

Figure 1.6: Thermal stability and optical images of the solid-state pouch cell at 0% and 100% SOC. Reproduced from [23].

Also, Rui *et al,*[24] explored the thermal runaway mechanisms of sulfide – based all – solid – state – batteries (ASSBs) by investigating two distinct thermal runaway pathways (gas – solid reactions and solid – solid reactions) by using different sulfide solid electrolytes: glassy – ceramic SEs (such as Li_3PS_4 and $Li_7P_3S_{11}$) and crystalline SEs (such as Li_6PS_5Cl and $Li_{10}GeP_2S_{12}$). Results showed that the glassy – ceramic SEs undergo gas – solid reactions at around 200°C, triggered by the release of oxygen from the NMC cathode, resulting in substantial heat and toxic sulfur dioxide (SO_2) gas generation. On the other hand, crystalline SEs remain stable against oxygen up to around 200°C but react with the decomposed products of the NMC cathode, such as transition – metal oxides and very little SO_2 gas, to give a solid – solid reaction pathway. Differential scanning calorimetry – mass spectrometry (DSC – MS) and other characterizations were used to validate the thermal runaway mechanisms. The gas – solid reaction pathway (observed in glassy – ceramic SEs) is characterized by the direct oxidation of the SE by oxygen released from the NMC cathode, producing SO_2 and substantial heat. In contrast, the solid – solid reaction pathway (observed in crystalline SEs) involves reactions with the solid decomposition products of the NMC cathode, resulting in different thermal failure behaviors.

1.4. Thesis Focus.

This thesis investigates the thermal runaway mechanism, reaction pathways, and the temperature rise in solid-state batteries, especially Li / Li_6PS_5Cl / NMC811 anode – cathode – electrolyte (ACE) samples using the differential scanning calorimetry (DSC). By examining the thermochemistry of these samples, the research aims to elucidate the

reaction pathways, and the temperature rise that leads to thermal runaway, a critical safety concern in solid – state battery technology. Furthermore, this thesis also explores the effect of small amounts of liquid electrolyte on the thermal behavior of these solid-state batteries, as shown in Figure 1.7. The findings from this research contribute to the broader knowledge base necessary for the development of safer and more efficient energy storage systems, particularly in applications where high energy density and thermal stability are paramount.

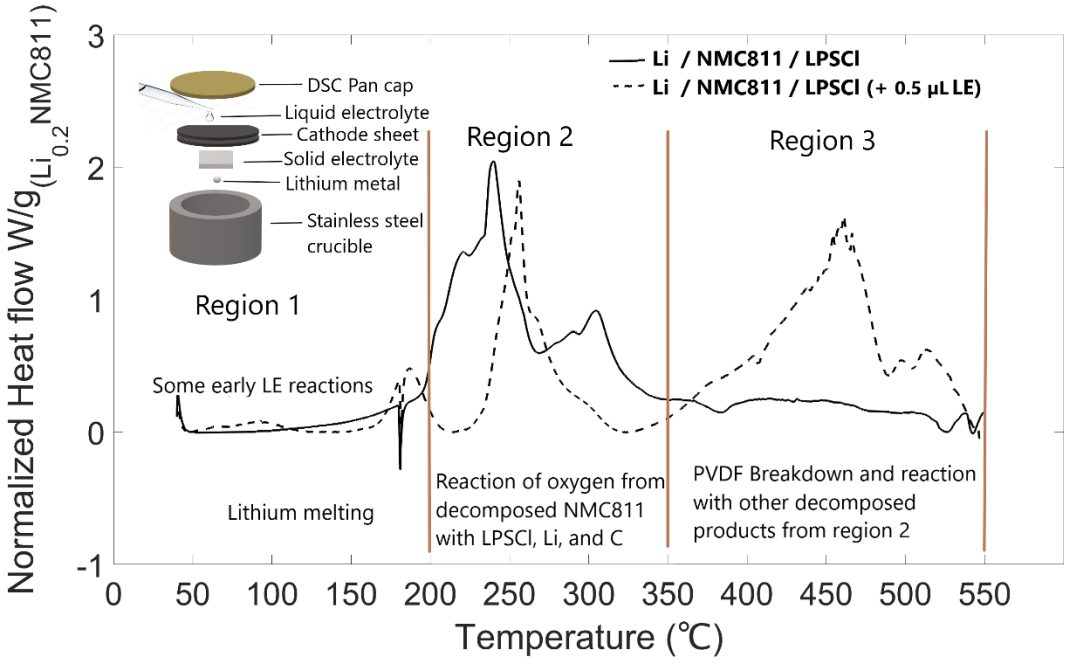

Figure 1.7: An overview of my research.

Chapter 2: Methodology

2.1. Materials Preparation.

Lithium Nickel Manganese Cobalt Oxide ($LiNi_{0.8}Mn_{0.1}Co_{0.1}O_2$) cathode sheets, commonly referred to NMC811 cathode, with a composition of 90% active material, 5% PVDF binder, and 5% conductive carbon, were purchased from NEI corporation and stored in the glovebox. Li metal sheets and ingots were purchased from MSE Supplies and Sigma Aldrich, respectively. The lithium ingots were stored in mineral oil to avoid being oxidized. Argyrodite Li_6PS_5Cl sulfide solid electrolyte powders, commonly referred to as LPSCl were purchased from Ampcera with particle size of ~1 µm, as shown in Figure 2.1. The powders were hot pressed (at 150 °C and 300 MPa for one hour) and cold pressed (at 20 °C and 300MPa for about ten minutes) in a 18mm custom made die, with a density of ~1.63 g/cm^3. The LPSCl pellets were fractured to obtain shards for DSC pans. Celgard separators were purchased from Celgard, and used in their pristine form.

Figure 2.1: Li_6PS_5Cl sulfide solid electrolyte pellet (0.870 mm thick and 0.5 – inch diameter).

2.2. Split Cell Preparation.

The split cell preparation was carried out in the glovebox. The purchased NMC811 cathode sheets, aluminum foils, and Lithium metal foils were punched into 18 mm diameter sheets. The Celgard separator was punched into 20 mm diameter sheet to adequately prevent contact of the anode and cathode materials. Both sides of the Lithium metal foil were scrapped to remove any oxidized layer deposited on the metal foil. The materials were layered into the split cell device in the following order from top to bottom: one sheet of the $LiNi_{0.8}Mn_{0.1}Co_{0.1}O_2$ sheets (with the current collector facing up), the Celgard separator, the Lithium metal disk, and the aluminum current collector. 4 – 5 drops of 1M $LiPF_6$ in EC/DEC (1:1 v/v) electrolyte was added on the lithium metal disk and on the Celgard separator. The NMC811 cathode sheet was charged CC / CV to 4.3 V vs Li^+ / Li in the split cell device to a lithium content of 0.2. The cathode sheet was removed from the split cell, rinsed with diethyl carbonate (DEC) about 10 times and dried at 70 °C in an oven under vacuum overnight to remove the liquid electrolyte salts.

2.3. Anode – Cathode – Electrolyte (ACE) Sample Preparation.

For the ACE sample preparation, two 4 mm diameter cathode sheets were used for the DSC tests. The ACE samples were assembled in a hermetically sealed stainless – steel pan (rated up to 200 bar), with around 0.15 mg lithium (cut from bulk lithium ingot) put at the base of the pan, followed by ~11 mg of LPSCl shard, and two sheets of the $Li_{0.2}$NMC811 (~ 4 mg with the current collectors facing down), as shown in Figure 2.2. Two sheets were used to match the capacity ratio of the lithium anode (N : P ratio of

1 : 1). The mass of the LPSCl shard used is very important because it reacts with other components of the cell up to 550 °C. Furthermore, the effect of liquid electrolyte on the ACE samples were also determined. In this case, varying amount of liquid electrolyte (0.1 µL, 0.5 µL, and 1 µL) were added to the top of the $Li_{0.2}$NMC811 sheet in the ACE sample assembly. The maximum volume of liquid electrolyte added was calculated based on the total volume of ACE samples within the DSC pan. To avoid exceeding the pan's maximum operating pressure, 20% of the remaining volume was allocated for the liquid electrolyte, accounting for the evolved gases from the thermal decomposition of ACE samples, which also contribute to pressure buildup. This limits the maximum liquid electrolyte volume to ~ 2 µL. The calculations are shown in Appendix A.5. In addition, a single cathode sheet has a capacity of about 0.25 mAh. As a commercial Li – ion cell (with a porous anode and separator, in addition to cathode) has an electrolyte : capacity ratio of about 1.3 g / Ah, that would translate to about 0.65 mg of electrolyte within our DSC pans (for two cathode sheets), or about 0.5 µL. Hence, the tests with 0.5 µL roughly match the electrolyte : capacity ratio expected in a cathode sheet alone.

2.4. Differential Scanning Calorimetry Measurements.

The sample and reference DSC pans were placed in the DSC equipment. The stainless – steel DSC pans were initially equilibrated at 40 °C for 15 minutes to ensure thermal uniformity.

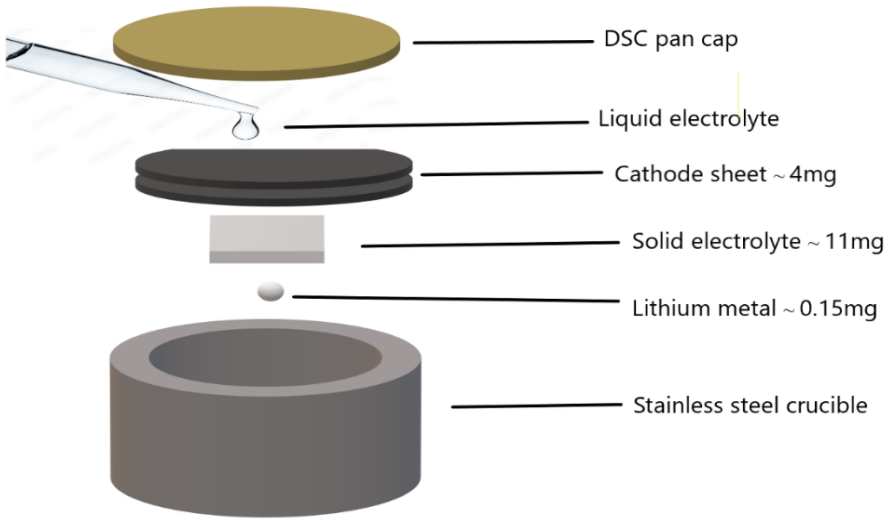

Figure 2.2: ACE Sample setup.

After equilibration, the pans were gradually heated to 550 °C at a ramp rate of 2°C / min to allow for the accurate measurement of the thermal transitions across the specified temperature range and minimize the effect of thermal lags from the pan on the measured heat, as the sample mass is very small compared to the pan mass.

2.5. Method of Integration.

To estimate the total heat released based on the variation in the different empty pan baselines (Figure 2.3a), the raw DSC heat flow is not subtracted from empty pan baseline. Instead, multiple points from the no – heat region of the raw heat flow curves are selected and fitted using the MATLAB algorithms I developed to form an integration baseline (Appendix A.1). This baseline is then used to correct the heat flow data, as shown in Figure 2.3b. Subsequently, the baseline – corrected heat flow is integrated across the exothermic regions to calculate the total heat released.

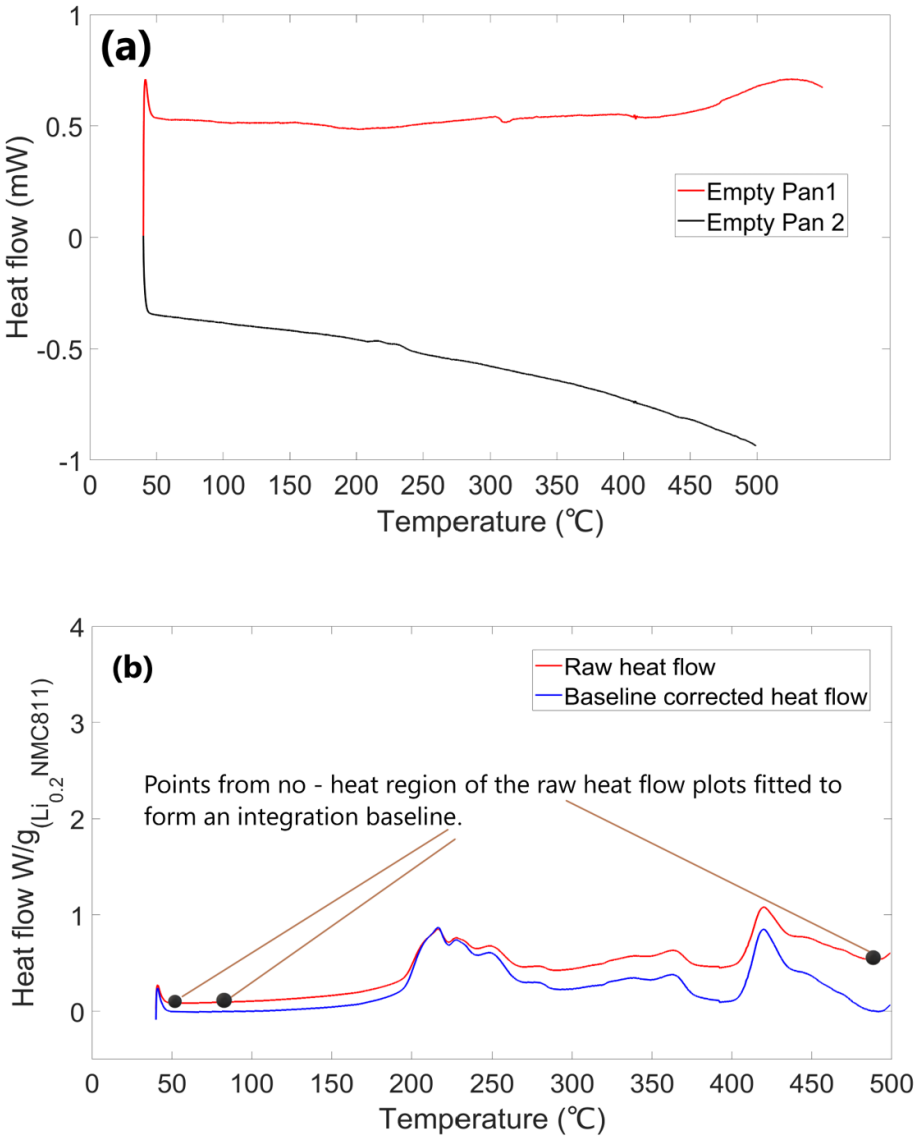

Figure 2.3: (a). Variations in the raw empty pan baselines. (b). Raw heat flow and the baseline – corrected heat flow.

Chapter 3: Results and Discussion

3.1. Component DSC Results

Conducting differential scanning calorimetry (DSC) tests for all components of the cell is important before performing the ACE sample DSC analyses to provide a comprehensive understanding of the thermal properties of each component, such as melting points, glass transition temperatures, and decomposition behavior, and predict how the materials behave when combined in an ACE sample. The DSC results (with the normalized figures) of the components are explained below.

3.1.1. $Li_{0.2}$NMC811 cathode sheet

Two 18 mm diameter sheets of $Li_{0.2}$NMC811 (with current collector facing down) were placed in a sealed DSC pan. Two DSC replicate tests were performed at a heating rate of 2 ℃ / min from 40 ℃ to 550 ℃. From Figure 3.1, there are exothermic peaks around 200 ℃, which are likely the decomposition of the cathode sheets. The exothermic peaks at 300 ℃ to 400 ℃ are likely from reactions of the oxygen from the decomposed $Li_{0.2}$NMC811 with carbon. Although there is no exothermic peak around 400 ℃, it is expected that PVDF breakdown and following exothermic reactions might be present at this temperature and above.

3.1.2. LPSCl Shard

Figure 3.2 shows three replicate DSC test results of LPSCl shard alone from 40 ℃ up to 550 ℃ at heating rates of 1 ℃ / min, 2 ℃ / min, and 4 ℃ / min, respectively. The LPSCl pellet was broken into shards and was sealed in a DSC pan. The result shows that LPSCl shows no obvious exothermic or endothermic peak up to 500 ℃,

highlighting its high thermal stability. Our result conforms with the results found in literature[24] (Appendix A.2).

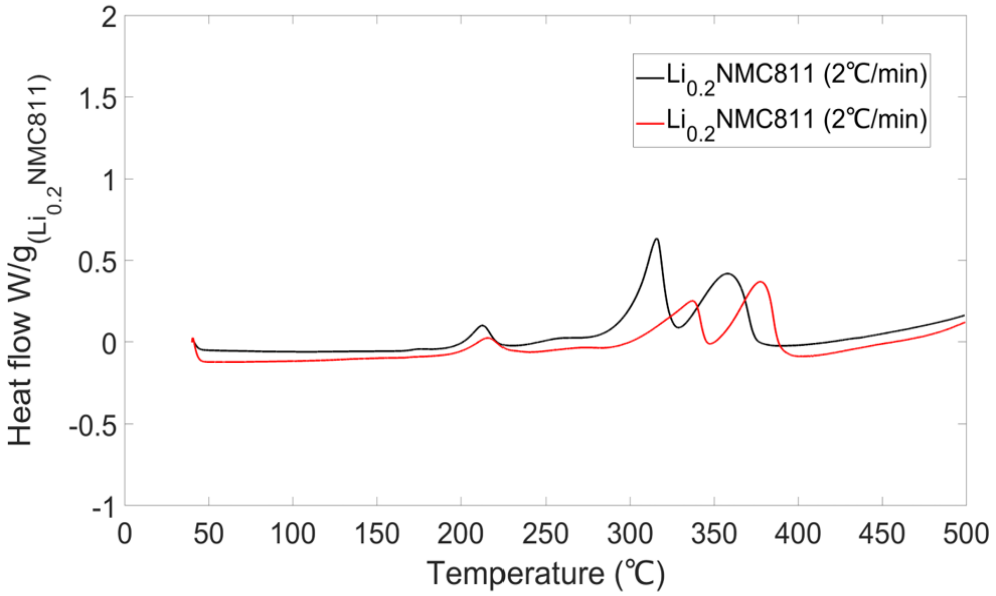

Figure 3.1: Raw DSC result of $Li_{0.2}$NMC811 cathode sheet.

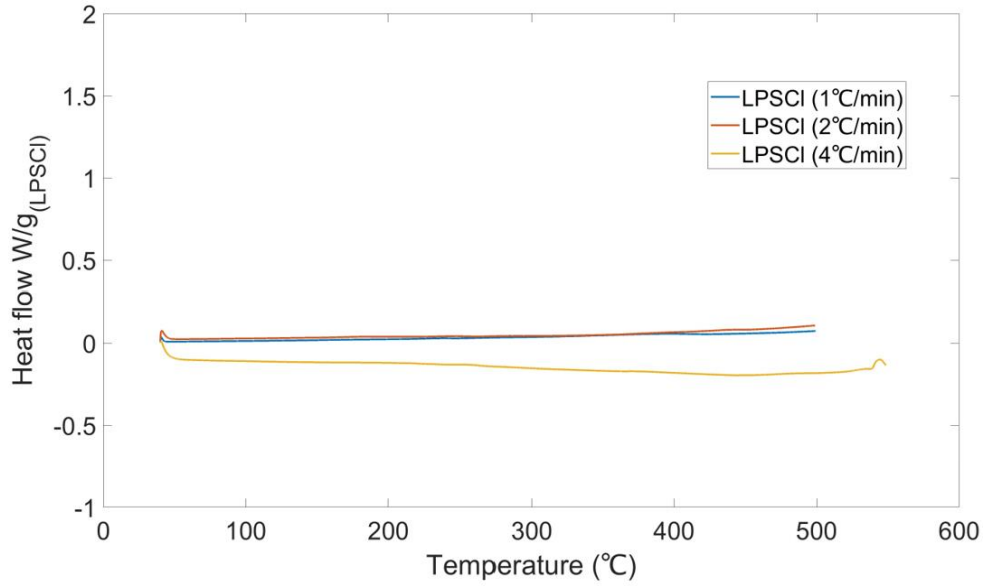

Figure 3.2: Raw DSC result of LPSCl shards.

3.1.3. $Li_{0.2}$NMC811 cathode sheet + LPSCl Shard

The DSC result of the three replicates of the component NMC811 + LPSCl shard is shown in Figure 3.3a. It is observed that, compared to the DSC result of $Li_{0.2}$NMC811 only (Figure 3.3b), there is a large exotherm around 200 ℃ to 300 ℃, which is likely due to the reaction of the LPSCl with oxygen released from decomposed $Li_{0.2}$NMC811, as seen in equation 1 (this gives reactants and products, but not exact stoichiometry):

$$O_2 + Li_6PS_5Cl \rightarrow S, SO_2, Li_3PO_4, LiCl \quad (1)$$

Also, at around 400℃, the PVDF in the $Li_{0.2}$NMC811 cathode sheet breaks down, releasing hydrogen fluoride gas (HF), which can react with the products in equation (1) to form the possible products shown in equation (2). The total heat generation from 50 ℃ to 550 ℃ is around 3100 – 3400 J/g $_{NMC811}$.

$$HF + S + SO_2 + Li_3PO_4 + LiCl \rightarrow H_2S, LiF, H_3PO_4, \ldots \quad (2)$$

3.1.4. Liquid electrolyte ($LiPF_6$ in EC: DEC: 1:1 v/v).

Figure 3.4 shows two replicates of the DSC result of 0.5 µL liquid electrolyte, $LiPF_6$ in EC: DEC (1:1 v/v) only. A small endotherm was observed at around 250 ℃, followed by two successive exotherms at around 275 ℃ and 280 ℃, respectively. The endotherm around 250 ℃ is likely due to electrolyte salt decomposition (equation 3). At 275 ℃, DEC may react with PF_5 from the decomposed $LiPF_6$ (equations 4). The heat generation from 50 ℃ to 550 ℃ is around 65 J/g $_{LE}$, as seen in Figure 3.4b.

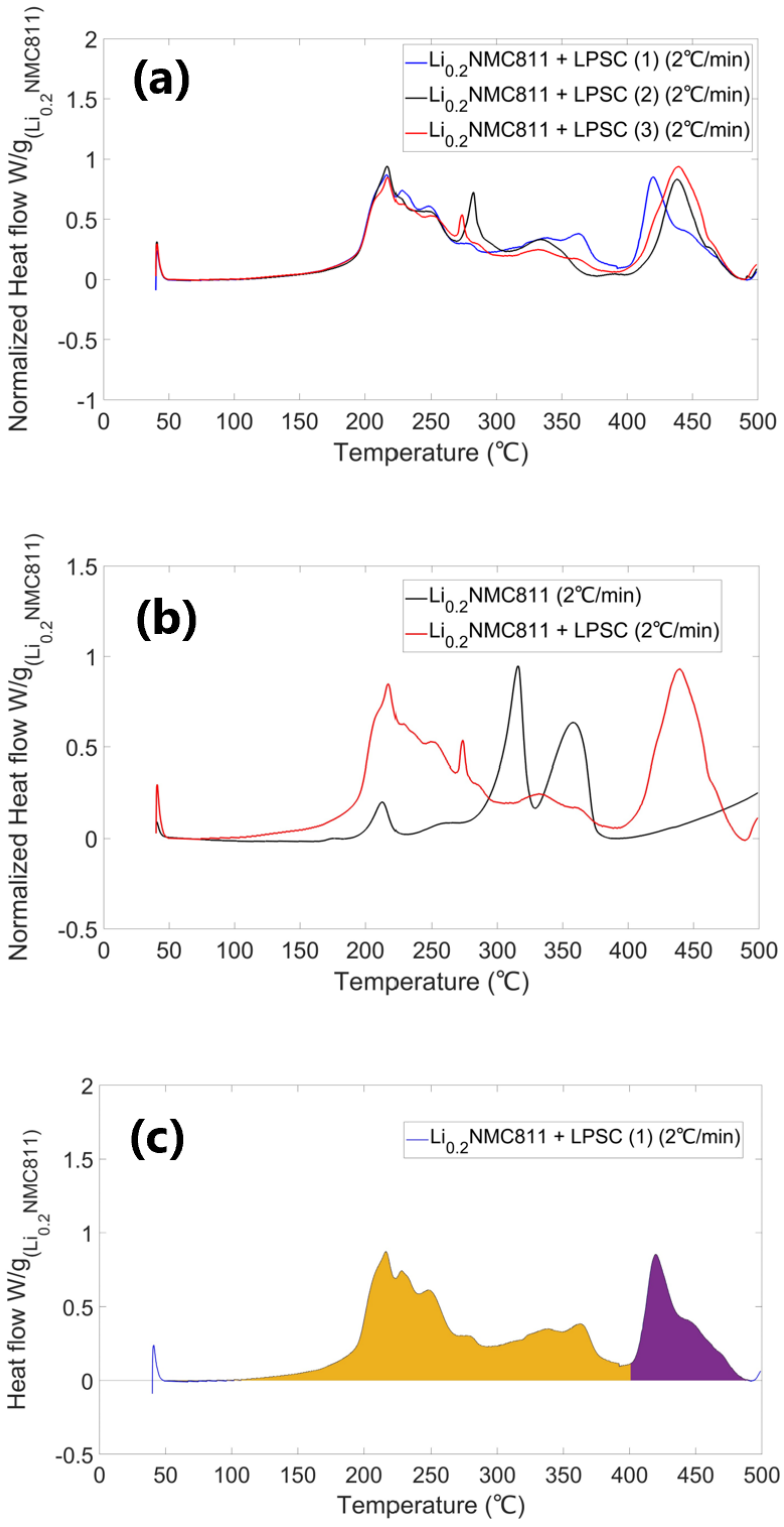

Figure 3.3: (a) Baseline – corrected DSC result of $Li_{0.2}$NMC811 cathode sheet + LPSCl Shard. (b) Comparison with $Li_{0.2}$NMC811 cathode sheet only. (c) Integrated area of $Li_{0.2}$NMC811 cathode sheet + LPSCl Shard.

$$LiPF_6 \rightarrow LiF + PF_5 \quad (3)$$

$$C_2H_5OCOOC_2H_5 + PF_5 \rightarrow C_2H_5OCOOPF_4 + HF + C_2H_4 \quad (4)$$

At 280 ℃, there may be a polymerization of EC, according to equation 5:

$$(CH_2O)_2CO \rightarrow [(CH_2CH_2O)_n\,COO]_m + CO_2 \quad (5)$$

As a result, our result conforms to the results of Roth *et al*[25] and Wang *et al*[26], as shown in Appendix A.3 and A.4, respectively.

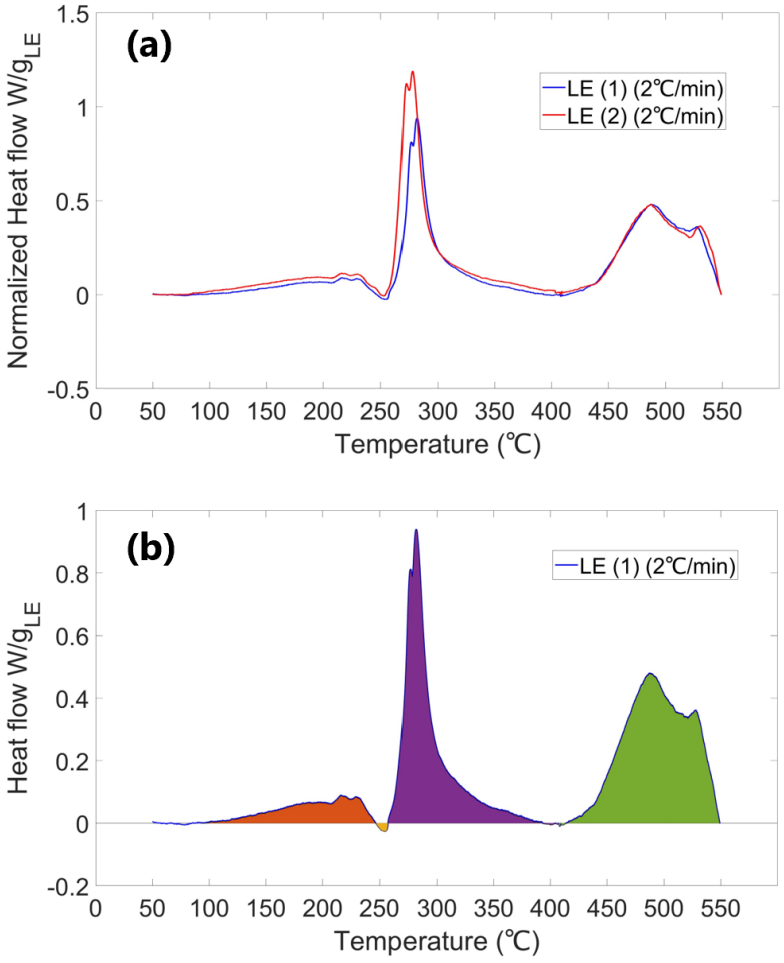

Figure 3.4: (a) Baseline - corrected DSC result of the liquid electrolyte. (b) Integrated DSC result of the liquid electrolyte.

3.1.5. $Li_{0.2}$NMC811 cathode sheet + Liquid Electrolyte

Two replicates of the DSC test of $Li_{0.2}$NMC811 cathode sheet + the liquid electrolyte were performed. The 0.5 µL LE was added on top of the two sheets of $Li_{0.2}$NMC811, with the cathode current collectors facing down, in a closed stainless – steel DSC pan. The DSC test was performed at 2 ℃ / min, and compared with $Li_{0.2}$NMC811 only with the result shown in Figure 3.5a. It is observed that the addition of the liquid electrolyte to the $Li_{0.2}$NMC811 sheets led to bigger exotherms around 180 ℃ to 250 ℃ compared to $Li_{0.2}$NMC81 only (Figure 3.5b), showing an increased heat production from the reaction of $Li_{0.2}$NMC811 and LE.

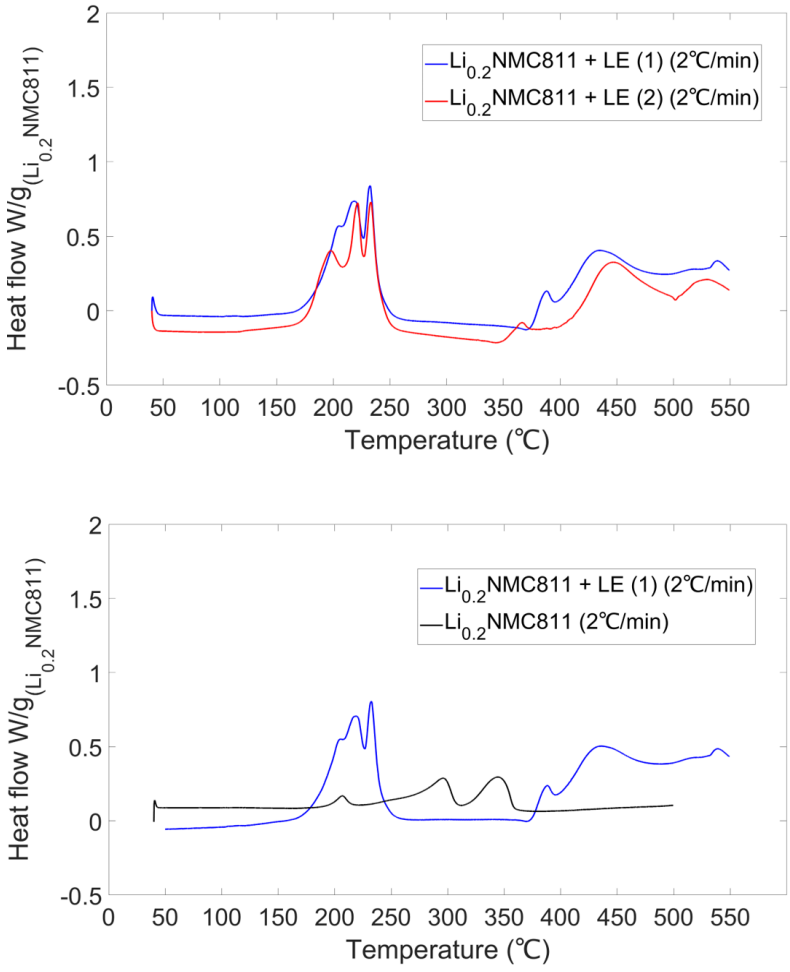

Figure 3.5: (a). Raw DSC result of the $Li_{0.2}$NMC811 cathode sheet with liquid electrolyte. (b) Raw DSC result of the comparison of $Li_{0.2}$NMC811 sheets with ($Li_{0.2}$NMC811 sheets + liquid electrolyte).

3.1.6. Li metal

Figure 3.6 shows the DSC result of lithium metal at a heating rate of 2 ℃ / min, from 40 ℃ to 500 ℃. As seen in the figure, there is an endotherm at around 183 ℃, which shows the melting point of lithium. After the lithium melting, there was no endothermic or exothermic peak.

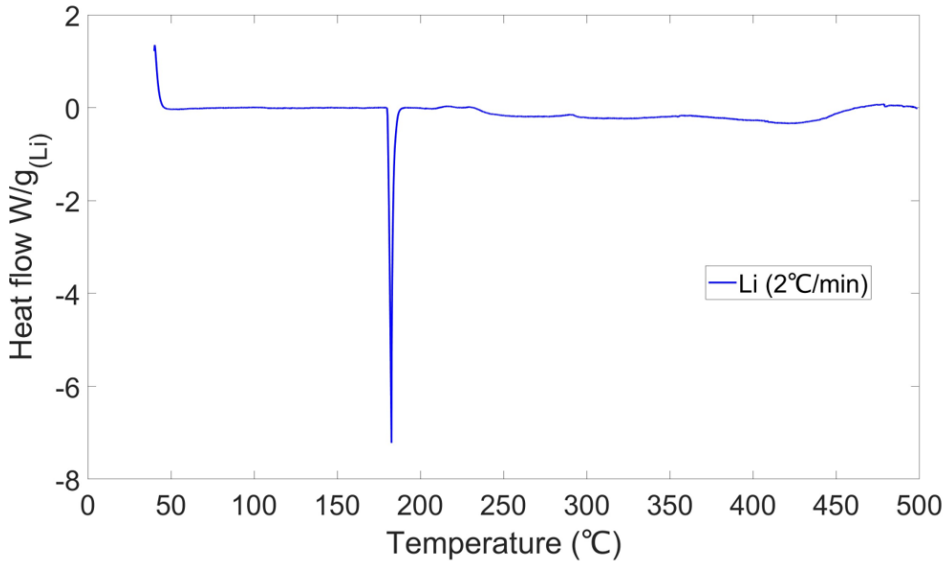

Figure 3.6: Raw DSC result of the Li metal.

3.1.7. Li metal + LPSCl Shard

Furthermore, the DSC tests for lithium ingot and LPSCl shard at 2 ℃ / min from 40 ℃ to 500 ℃ were performed. It was observed that there was no visible exothermic or endothermic peak throughout the test as shown in Figure 3.7, which indicates that there

is limited reactivity between the lithium metal and the LPSCl. This was also confirmed by Yang *et al.*[23].

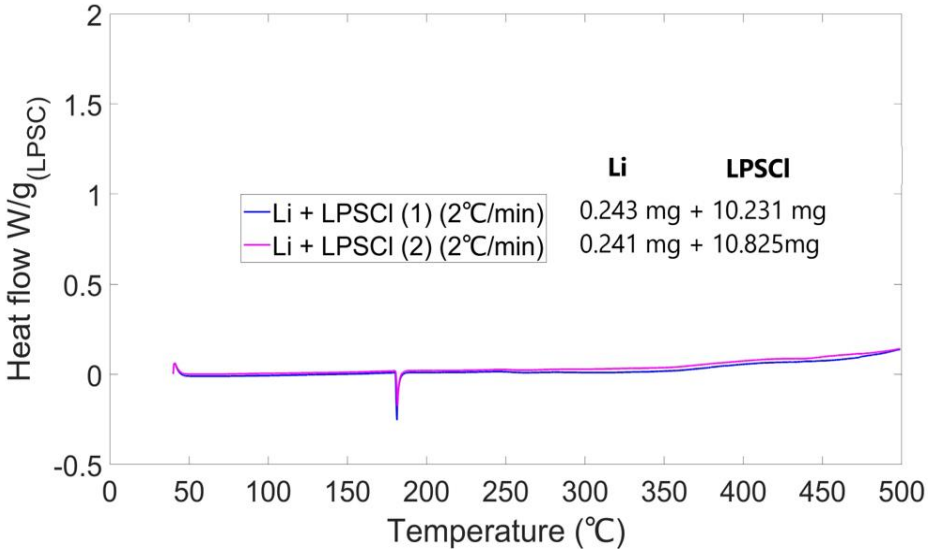

Figure 3.7: Raw DSC result of the reaction of lithium with LPSCl shard.

3.2. ACE Sample DSC Results

ACE sample DSC tests are essential in evaluating the combined thermal behavior of all the components. While component DSC tests provide insight into the thermal properties of each component, the ACE sample DSC analysis reveals how these materials interact when combined together. The DSC results of the ACE samples with hot – pressed and cold – pressed LPSCl shards are discussed below.

3.2.1. ACE Sample (NMC811 + Hot – pressed LPSCl + Li metal)

4 repeated runs of the DSC tests were performed for the ACE sample (Li / hot – pressed LPSCl / $Li_{0.2}$NMC811) from 40 ℃ to 550 ℃ with a heating rate of 2 ℃ / min (Figure 3.8a) with their respective cumulative heat flows (Figure 3.8b). It is observed that after

the lithium melting around 180 ℃, there is a broad exothermic peak from around 200 ℃ to 350 ℃, which is likely due to the reactions between oxygen from decomposed $Li_{0.2}$NMC811 and the hot – pressed LPSCl. However, there is no exothermic peak around 400 ℃ to 500 ℃ in the PVDF breakdown region, which may indicate there are no species still present that are able to undergo exothermic reactions with the PVDF breakdown products.

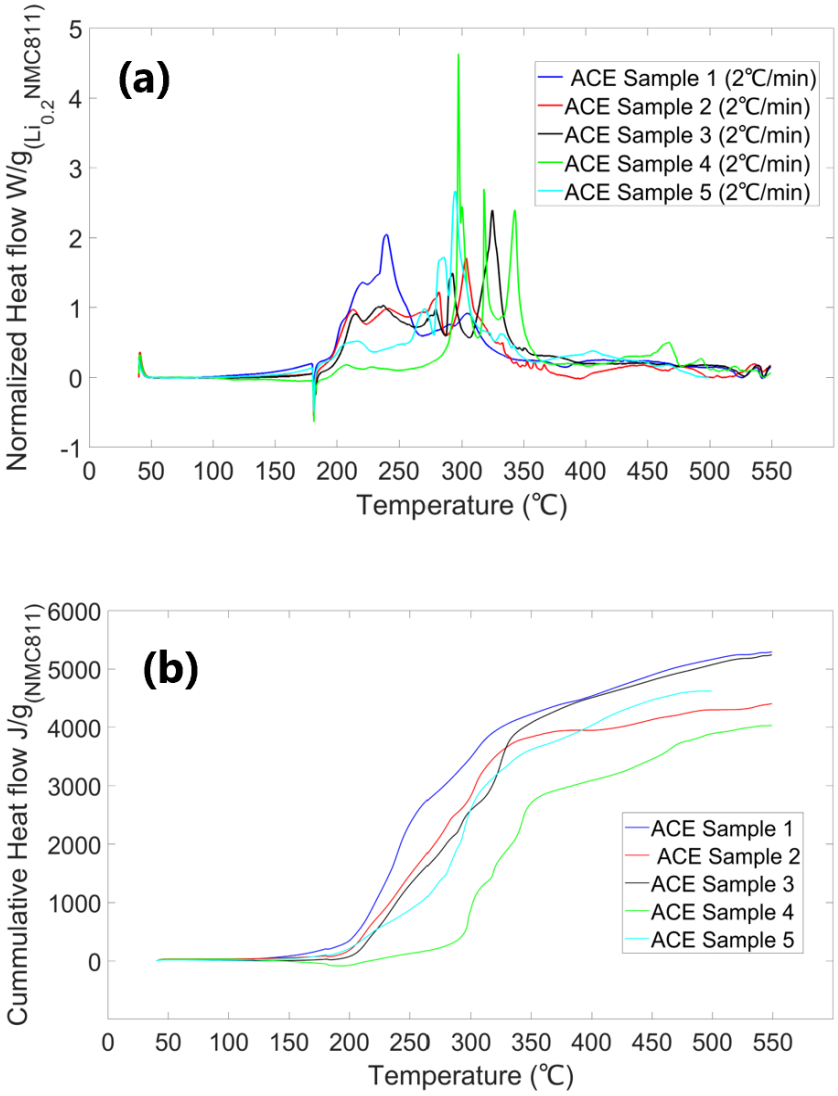

Figure 3.8: (a) Baseline – corrected DSC result of the ACE sample with hot – pressed LPSCl shard. (b) Cumulative heat flow of the ACE sample.

3.2.2. ACE Sample (NMC811 + Cold – pressed LPSCl + Li metal)

The hot – pressed LPSCl shard was replaced with cold – pressed LPSCl shards in the ACE sample to understand the effect of the heat treatment of the LPSCl pellet on the heat generation of the ACE sample. Two repeated DSC runs were performed. From Figure 3.9a, there is an exothermic peak immediately after lithium melting to around 400 ℃, compared to the hot – pressed LPSCl ACE sample, leading to similar heat generation. Figure 3.9b shows the cumulative heat flows of the ACE samples.

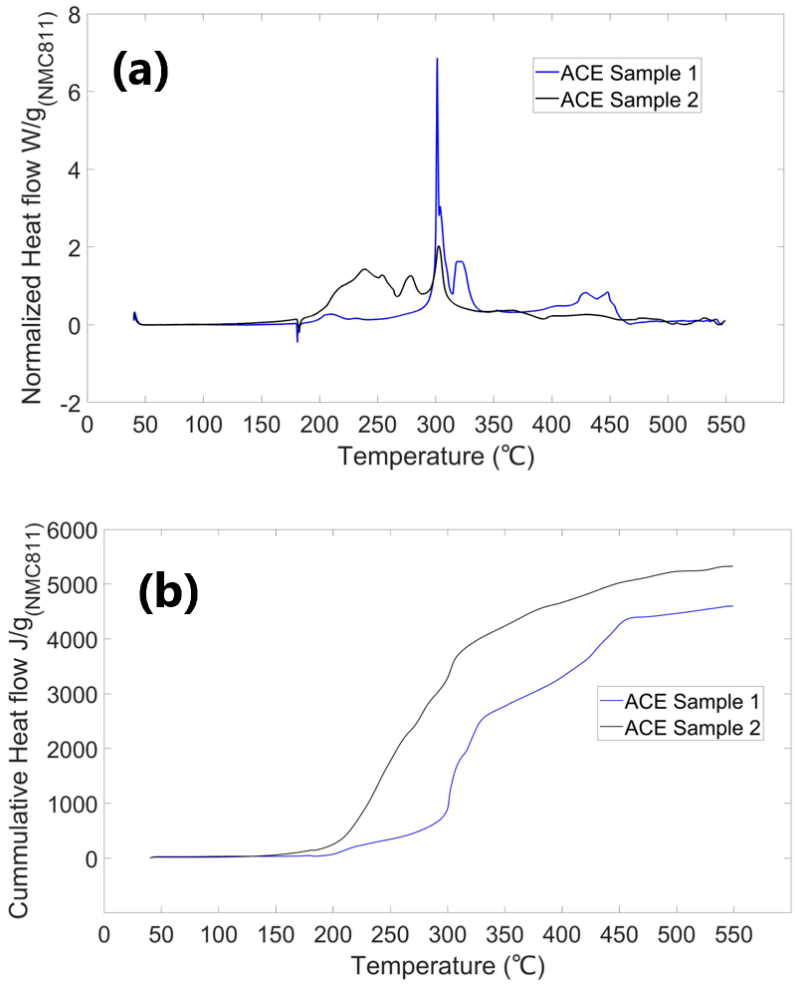

Figure 3.9: (a). Baseline – corrected DSC result of the ACE samples with cold – pressed LPSCl shard. (b). Cumulative heat flow of the ACE samples.

3.3. Effect of Liquid Electrolyte on the Heat Generation

Liquid electrolyte (1M $LiPF_6$ (EC : DEC 1:1 v/v)) was added to the Li / hot – pressed LPSCl / NMC811 ACE sample to further understand its effect on the thermal runaway mechanism. Here, various amounts of the liquid electrolyte were added to the cathode active material in the closed DSC pan. Figure 3.10 shows the DSC result of the ACE samples with 0.1 µL, 0.5 µL, and 1 µL of liquid electrolyte, respectively. It is observed that there is an increase in the exothermic peak of the DSC result around 100 ℃ as the liquid electrolyte introduced increased. Also, there are exothermic peaks from around 180 ℃ to 350 ℃, which may be attributed to the reaction of the decomposed electrolyte with the decomposed product of the $Li_{0.2}$NMC811 cathode sheets and LPSCl shard. At around 450 ℃, there is an exothermic peak, which is likely due to the PVDF breakdown and reaction with other decomposed products, which is not evident in the ACE samples without liquid electrolyte.

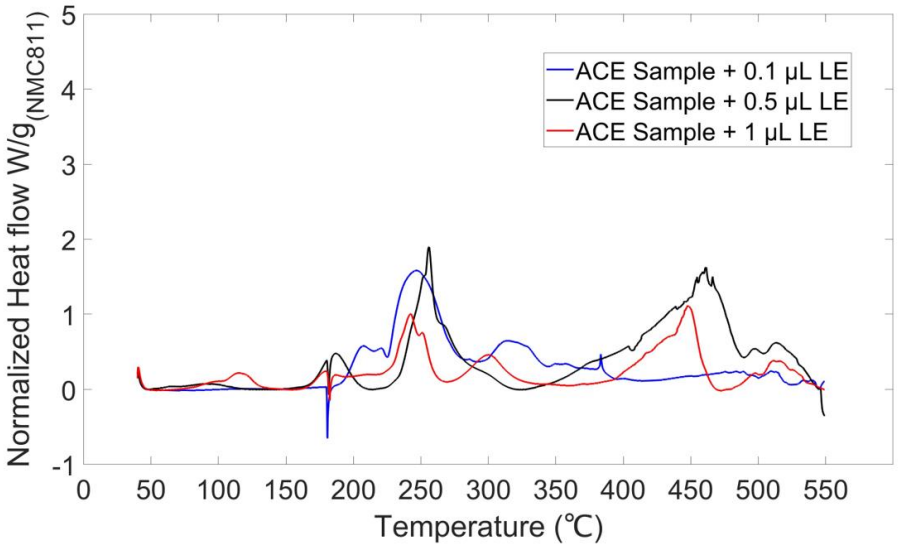

Figure 3.10: Baseline – corrected DSC result of the ACE sample with varying amounts of liquid electrolyte.

To further understand the reaction mechanism, the DSC tests of the ACE samples (without and with 0.5 µL liquid electrolyte) were performed up to 350 ℃ with a lithium remelt test from 170 ℃ to 190 ℃. After the lithium remelt test, it is observed that the lithium has completely reacted with the other components at 350 ℃, for the ACE sample without liquid electrolyte (Figure 3.11a). However, for the ACE sample with 0.5 µL liquid electrolyte, only about 70% of the lithium metal has been consumed (Figure 3.11b).

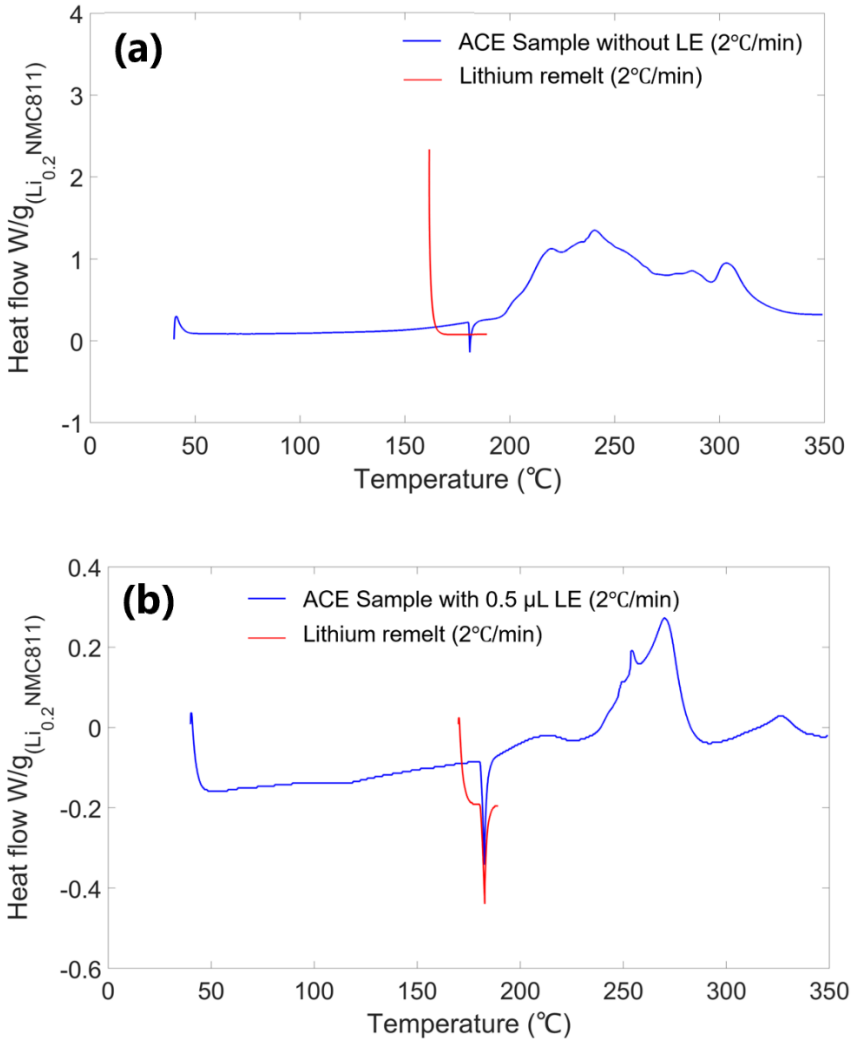

Figure 3.11: Raw DSC result of the ACE sample (a) without and (b) with 0.5 µL liquid electrolyte.

Based on the above results, it is observed that the addition of the liquid electrolyte lowers the onset temperature and shifts the heat release to higher temperatures, while the total heat released remains in a similar range. Compared to a Li – ion material set, the onset temperature is higher for the solid-state material sets, but the total heat release is similar, as shown in Table 1.

For a 350 $\frac{Wh}{kg}$ cell with 3.8 V, we have 92 Ah per 1000 g_{cell}

Assume 0.2 $\frac{Ah}{g_{NMC811}}$ = 330 g_{NMC811} per 1000 g_{cell}.

For a heat generation of 4000 $\frac{J}{g_{NMC811}}$,

Therefore 4 $\frac{MJ}{g_{NMC811}} \times \frac{330\ g_{NMC811}}{1000\ g_{cell}}$ = 1320 $\frac{J}{g_{cell}}$

Assuming the heat capacity is 1 $\frac{J}{g_{cell}K}$,

4000 $\frac{J}{g_{NMC811}}$ = 1320 $\frac{J}{g_{cell}}$ / 1 $\frac{J}{g_{cell}K}$ = 1320 ℃

The table below shows the comparison of the onset temperature, heat release, and adiabatic temperature rise of the tested ACE samples with and without liquid electrolyte. For the ACE samples with varying amount of liquid electrolyte, it is observed that the onset temperature of the ACE samples is lowered from ~ 190 ℃ to ~ 80 ℃ as the amount of added liquid electrolyte increases from 0.1 µL to 1 µL. However, the total heat released, and the adiabatic temperature rise are in the same range. For the ACE samples with hot – pressed and cold – pressed LPSCl, their onset temperatures remained the same. Moreover, their heat generation and adiabatic temperature rise are within the same range. Based on the results, it can be deduced that there is no obvious trend in how the amount of liquid electrolyte affects the total heat

release. The only effect of the liquid electrolyte appears to be a shift in heat release to higher temperatures. The significant variability in the heat flow results may indicate that the complexity of the ACE samples, including a large number of components and the importance of the lithium metal passivation, results in inherently stochastic reaction paths.

Table 1: Comparison of the onset temperature, heat release, and adiabatic temperature rise of different battery chemistries.

Battery Chemistries	**Onset Temperature of Exotherm (°C)**	**Total Heat (J/g_{NMC811}) ~50 °C to ~ 550 °C**	**Adiabatic temperature rise (°C)**
Li / LPSCl / NMC811 (hot pressed LPSC)	~ 190 °C	4000 – 5300	1300 – 1750
Li / LPSCl / NMC811 (cold pressed LPSC)	~ 190 °C	4600 – 5300	1500 – 1750
Li / LPSCl / NMC811 + 1 µL LE	~ 80 °C	3500 – 5000	1150 – 1650
Li / LPSCl / NMC811 + 0.5 µL LE	~ 165 °C	2600 – 5400	860 – 1800
Li / LPSCl / NMC811 + 0.1 µL LE	~ 190 °C	3400 – 4300	1100 – 1400

Chapter 4: Conclusion

4.1. Results Summary

The thermal runaway and quantitative heat generation in solid – state battery, especially the ACE (Li / hot – pressed LPSCl / NMC811) samples were investigated using the differential scanning calorimetry (DSC) tests. The DSC result of LPSCl alone showed no obvious exothermic or endothermic peak up to 500 ℃ highlighting its excellent thermal stability. However, when incorporated in an ACE sample, it reacts with oxygen from the decomposition $Li_{0.2}$NMC811, resulting in a large exotherm around 200 ℃ to 350 ℃, giving a heat generation of around 4000 - 5300 J/g $_{NMC811}$. When compared to an ACE sample with cold – pressed LPSCl (4600 – 5300 J/g $_{NMC811}$), they are within the same range.

To further understand the effect of liquid electrolyte on the thermal runaway of all – solid – state cells, small amounts of liquid electrolyte were added to the ACE samples. It is observed that the addition of the liquid electrolyte lowered the onset temperature and shifted the heat release to higher temperatures. However, the total heat generation remained within a similar range. Compared to a Li – ion material set, the onset temperature is higher for the solid-state material sets, but the total heat release is similar. This analysis highlights that while solid-state batteries offer enhanced performance due to their higher energy densities, they present significant safety concerns. As a result, they may not be as safe as traditional lithium – ion batteries, as their heat generation is higher. These findings are crucial for understanding the temperature rise, heat generation, and safety of solid – state batteries.

4.2. Limitations to Current Work

This research presents some limitations that impact the comprehensiveness of the result findings. First, the reliance on Differential Scanning Calorimetry (DSC) only as the primary analytical tool limits the scope of data collection. While DSC is highly effective at measuring thermal transitions, it may not capture other critical factors, such as electrochemical reactions that also contribute to the thermal runaway of solid – state batteries. The results from the DSC measurements may not fully translate to large – format cells where external factors also influence the thermal behavior and safety. In a commercial cell, the cell layers are designed with optimized electrode and electrolyte configurations to facilitate efficient ion transport, enhancing electrochemical performance. Meanwhile, in a DSC pan, the layered configuration is not engineered for electrochemical processes, resulting in less efficient transport between layers. Also, the sensitivity of LPSCl to atmospheric exposure makes accurate post-calorimetry analysis (such as X-ray Photoelectron Spectroscopy (XPS) and X-ray Diffraction (XRD)) challenging.

Another significant constraint in this study is the inability of our Differential Scanning Calorimetry (DSC) setup to perform gas chromatography-mass spectrometry (GC – MS) analysis of gases evolved during thermal decomposition. The DSC pans used in this research are hermetically sealed to prevent material loss during heating. While this ensures accurate thermal measurements, it limits the analysis of volatile gases released during thermal runaway, which are crucial for understanding the full decomposition reactions. Lastly, the laboratory environment used for this research differs from real –

world operating conditions. The controlled laboratory setting does not account for external factors which could significantly affect battery safety during operation in electric vehicles or grid – scale energy storage systems.

4.3. Recommendations and Future Work

To address the limitations identified in this work, the following recommendations and future work are highlighted. Further post – calorimetry characterization techniques, such as in-situ XPS or XRD, should be employed to monitor real-time reactions within the battery, thus providing a clearer understanding of the degradation processes.

To enhance the understanding of thermal runaway and reaction mechanisms, future research should incorporate Gas Chromatography-Mass Spectrometry (GC – MS) analysis with Differential Scanning Calorimetry (DSC). This would require a modification of the DSC setup, allowing for the collection and analysis of evolved gases during thermal decomposition. By coupling GC – MS with DSC, the study could identify critical gas – phase reactions that contribute to thermal runaway.

Future research could also investigate the use of silicon anodes as a potential replacement for lithium metal in studying the thermal runaway behavior of ACE samples. Given the growing interest in silicon anodes for next – generation energy SSBs, incorporating them into future thermal runaway studies would be a logical step toward developing safer, high – performance solid – state batteries.

Appendices

A.1: Sample MATLAB Algorithms for fitting and integrating raw DSC heat flow data.

```
close all
clear
% ACE sample with 1uL LE

MC_LE1 = readmatrix ('C:\Users\dapot\OneDrive\Documents\UMD PhD\Paul
Albertus Group\joined\LPSC\2024\June 2024\MC with LE 1uL\2024-04-12 Full
Microcell with 1uL LE.csv');
MC_LE2 = readmatrix ('C:\Users\dapot\OneDrive\Documents\UMD PhD\Paul
Albertus Group\joined\LPSC\2024\June 2024\MC with LE 1uL\2024-05-22 Full
Microcell 1 w LE 1uL DSC2A-02873.csv');
MC_LE3 = readmatrix ('C:\Users\dapot\OneDrive\Documents\UMD PhD\Paul
Albertus Group\joined\LPSC\2024\June 2024\MC with LE 1uL\2024-05-22 Full
Microcell 2 w LE 1uL DSC2A-02873.csv');

total_mass = [14.972; 16.792; 16.229];
MC_LE1 (:,3) = MC_LE1 (:, 3).*(total_mass (1)); %mW
MC_LE2 (:,3) = MC_LE2 (:, 3).*(total_mass (2)); %mW
MC_LE3 (:,3) = MC_LE3 (:, 3).*(total_mass(3)); %mW

figure (1)
plot (MC_LE1(17:153016,2), MC_LE1(17:153016,3));
a(1) = 3402; a(2) = 85631; a(3) = 152996;
nmc_f = polyfit ([MC_LE1(a(1),2); MC_LE1(a(2),2);
MC_LE1(a(3),2)],[MC_LE1(a(1),3); MC_LE1(a(2),3); MC_LE1(a(3),3)],2);
nmc_f1 = polyval(nmc_f,MC_LE1(17:153016,2));
nmc_f2 = MC_LE1(17:153016,3) - nmc_f1;

figure (2)
plot (MC_LE2(18:153016,2), MC_LE2(18:153016,3));
b(1) = 4467; b(2) = 33241; b(3) = 129799; b(4) = 152920;
nmc_fb = polyfit ([MC_LE2(b(1),2); MC_LE2(b(2),2); MC_LE2(b(3),2);
MC_LE2(b(4),2)],[MC_LE2(b(1),3); MC_LE2(b(2),3); MC_LE2(b(3),3);
MC_LE2(b(4),3)],2);
nmc_fb1 = polyval(nmc_fb,MC_LE2(18:153016,2));
nmc_fb2 = MC_LE2(18:153016,3) - nmc_fb1;

figure (3)
plot (MC_LE3(18:153017,2),MC_LE3(18:153017,3));
c(1) = 3487; c(2) = 26264; c(3) = 51229; c(4) = 86712; c(5) = 152298;
nmc_fc = polyfit ([MC_LE3(c(1),2); MC_LE3(c(2),2); MC_LE3(c(3),2);
MC_LE3(c(4),2); MC_LE3(c(5),2)],[MC_LE3(c(1),3); MC_LE3(c(2),3);
MC_LE3(c(3),3); MC_LE3(c(4),3); MC_LE3(c(5),3)],4);
nmc_fc1 = polyval(nmc_fc,MC_LE3(18:153017,2));
nmc_fc2 = MC_LE3 (18:153017,3) - nmc_fc1;
```

```
figure (1)
plot (MC_LE1(17:153016,2),nmc_f2);
a(6) = 3565; a(7) = 43066; a(8) = 85631; a(9)= 152996;
Area_A = trapz(MC_LE1 (a(6): a(9),2), nmc_f2 (a(6): a(9),1) - nmc_f2
(a(6),1)).*(30/(4.011*0.7));
Area1a = trapz(MC_LE1 (a(6): a(7),2), nmc_f2 (a(6): a(7),1) - nmc_f2
(a(6),1)).*(30/(4.011*0.7));
Area1b = trapz(MC_LE1 (a(7): a(8),2), nmc_f2 (a(7): a(8),1) - nmc_f2
(a(6),1)).*(30/(4.011*0.7));
Area1c = trapz(MC_LE1 (a(8): a(9),2), nmc_f2 (a(8): a(9),1) - nmc_f2
(a(6),1)).*(30/(4.011*0.7));

figure (2)
plot (MC_LE2(18:153016,2),nmc_fb2);
b(6) = 7758; b(7) = 42815; b(8)= 129799; b(9) = 152995;
Area_B = trapz(MC_LE2 (b(6): b(9),2), nmc_fb2 (b(6): b(9),1) - nmc_fb2
(b(6),1)).*(30/(3.912*0.7));
Area2a = trapz(MC_LE2 (b(6): b(7),2), nmc_fb2 (b(6): b(7),1) - nmc_fb2
(b(6),1)).*(30/(3.912*0.7));
Area2b = trapz(MC_LE2 (b(7): b(8),2), nmc_fb2 (b(7): b(8),1) - nmc_fb2
(b(6),1)).*(30/(3.912*0.7));
Area2c = trapz(MC_LE2 (b(8): b(9),2), nmc_fb2 (b(8): b(9),1) - nmc_fb2
(b(6),1)).*(30/(3.912*0.7));

figure (3)
plot (MC_LE3(18:153017,2), nmc_fc2);
c(6) = 6088; c(7) = 42839; c(8) = 85371; c(9) = 152146;
Area_C = trapz (MC_LE3 (c(6): c(9),2), nmc_fc2 (c(6): c(9),1) - nmc_fc2
(c(6),1)).*(30/(3.858*0.7));
Area3a = trapz (MC_LE3 (c(6): c(7),2), nmc_fc2 (c(6): c(7),1) - nmc_fc2
(c(6),1)).*(30/(3.858*0.7));
Area3b = trapz (MC_LE3 (c(7): c(8),2), nmc_fc2 (c(7): c(8),1) - nmc_fc2
(c(6),1)).*(30/(3.858*0.7));
Area3c = trapz (MC_LE3 (c(8): c(9),2), nmc_fc2 (c(8): c(9),1) - nmc_fc2
(c(6),1)).*(30/(3.858*0.7));

figure (1)
plot (MC_LE1(17:153000,2), (nmc_f2 (17:153000,1) - nmc_f2
(a(2),1)) ./(4.011*0.7), 'b', 'linewidth',1);
xlabel ('Temperature (°C)', 'fontsize', 20);
ylabel ('Heat flow W/g_{(NMC811)}', 'fontsize', 20);
hold on
area (MC_LE1 (a(6): a(7),2), (nmc_f2 (a(6): a(7),1) - nmc_f2
(a(6),1))./(4.011*0.7));
area (MC_LE1 (a(7): a(8),2), (nmc_f2 (a(7): a(8),1) - nmc_f2
(a(6),1))./(4.011*0.7));
area (MC_LE1 (a(8): a(9),2), (nmc_f2 (a(8): a(9),1) - nmc_f2
(a(6),1))./(4.011*0.7));
ax=gca;
ax.FontSize=30;
ylim ([-0.5, 4]);
xticks(0:50:550);
legend ('Full Microcell 1 + 1 µL LE (2°C/min)');
```

```
% Convert heat flow (mW) to J/g by integrating and dividing by heating rate
(assuming 2°C/min)
heating_rate = 2 / 60; % °C/s
cum_energyA = cumtrapz(MC_LE1(17:153016, 2), nmc_f2) / (4.011 * 0.7 *
heating_rate);
% Plot the cumulative energy vs temperature
figure (2)
plot(MC_LE1(17:153016, 2), cum_energyA, 'b', 'linewidth', 1);
xlabel ('Temperature (℃)', 'fontsize', 20);
ylabel ('Cummulative Heat flow J/g_{(NMC811)}', 'fontsize', 20);
ax=gca;
ax.FontSize=30;
yticks(0:500:6000);
xticks(0:50:550);
legend ('Cumulative Heat Flow J/g for MC1 + 1 µL LE');


figure (3)
plot (MC_LE2(18:152999,2), (nmc_fb2 (18:152999,1) - nmc_fb2
(b(2),1)) ./(3.912*0.7), 'r', 'linewidth',1);
xlabel ('Temperature (℃)', 'fontsize', 20);
ylabel ('Heat flow W/g_{(NMC811)}', 'fontsize', 20);
hold on
area (MC_LE2 (b(6): b(7),2), (nmc_fb2 (b(6): b(7),1) - nmc_fb2
(b(6),1))./(3.912*0.7));
area (MC_LE2 (b(7): b(8),2), (nmc_fb2 (b(7): b(8),1) - nmc_fb2
(b(6),1))./(3.912*0.7));
area (MC_LE2 (b(8): b(9),2), (nmc_fb2 (b(8): b(9),1) - nmc_fb2
(b(6),1))./(3.912*0.7));
ax=gca;
ax.FontSize=30;
ylim ([-0.5, 4]);
xticks(0:50:550);
legend ('Full Microcell 2 + 1 µL LE (2℃/min)');
% Convert heat flow (mW) to J/g by integrating and dividing by heating rate
(assuming 2°C/min)
heating_rate = 2 / 60; % °C/s
cum_energyB = cumtrapz(MC_LE2(18:153016, 2), nmc_fb2) / (3.912 * 0.7 *
heating_rate);
% Plot the cumulative energy vs temperature
figure (4)
plot(MC_LE2(18:153016, 2), cum_energyB, 'r', 'linewidth', 1);
xlabel ('Temperature (℃)', 'fontsize', 20);
ylabel ('Cummulative Heat flow J/g_{(NMC811)}', 'fontsize', 20);
ax=gca;
ax.FontSize=30;
yticks(0:500:6000);
xticks(0:50:550);
legend ('Cumulative Heat Flow J/g for MC2 + 1 µL LE');


figure (5)
plot (MC_LE3(18:152998,2), (nmc_fc2 (18:152998,1) - nmc_fc2
(c(2),1)) ./(3.858*0.7),'k', 'linewidth',1);
```

```
hold on
area (MC_LE3(c(6): c(7),2), (nmc_fc2 (c(6): c(7),1) - nmc_fc2
(c(6),1))./(3.858*0.7));
area (MC_LE3(c(7): c(8),2), (nmc_fc2 (c(7): c(8),1) - nmc_fc2
(c(6),1))./(3.858*0.7));
area (MC_LE3(c(8): c(9),2), (nmc_fc2 (c(8): c(9),1) - nmc_fc2
(c(6),1))./(3.858*0.7));
xlabel ('Temperature (°C)', 'fontsize', 20);
ylabel ('Heat flow W/g_{(NMC811)}', 'fontsize', 20);
ax=gca;
ax.FontSize=30;
ylim ([-0.5, 4]);
xticks(0:50:550);
legend ('Full Microcell 3 + 1 µL LE (2°C/min)');
% Convert heat flow (mW) to J/g by integrating and dividing by heating rate
(assuming 2°C/min)
heating_rate = 2 / 60; % °C/s
cumm_energyC = cumtrapz(MC_LE3(18:153017, 2), nmc_fc2) / (3.858 * 0.7 *
heating_rate);
% Plot the cumulative energy vs temperature
figure (6)
plot(MC_LE3(18:153017, 2), cumm_energyC, 'k', 'linewidth', 1);
xlabel ('Temperature (°C)', 'fontsize', 20);
ylabel ('Heat flow J/g_{(NMC811)}', 'fontsize', 20);
ax=gca;
ax.FontSize=30;
yticks(0:500:6000);
xticks(0:50:550);
legend ('Cumulative Heat Flow J/g for MC3 + 1 µL LE');

figure (7)
plot(MC_LE1(17:153016, 2), cum_energyA, 'b', 'linewidth', 1);
hold on
plot(MC_LE2(18:153016, 2), cum_energyB, 'r', 'linewidth', 1);
hold on
plot(MC_LE3(18:153017, 2), cumm_energyC, 'k', 'linewidth', 1);
xlabel ('Temperature (°C)', 'fontsize', 20);
ylabel ('Cummulative Heat flow J/g_{(NMC811)}', 'fontsize', 20);
ax=gca;
ax.FontSize=30;
yticks(0:1000:7000);
xticks(0:50:550);
legend ('MC1 + 1 µL LE', 'MC2 + 1 µL LE', 'MC3 + 1 µL LE');

figure (8)
plot (MC_LE1(17:153000,2), (nmc_f2 (17:153000,1) - nmc_f2
(a(2),1)) ./(4.011*0.7), 'b', 'linewidth',2);
hold on
plot (MC_LE2(18:152999,2), (nmc_fb2 (18:152999,1) - nmc_fb2
(b(2),1)) ./(3.912*0.7), 'r', 'linewidth',2);
hold on
plot (MC_LE3(18:152998,2), (nmc_fc2 (18:152998,1) - nmc_fc2
(c(2),1)) ./(3.858*0.7),'k', 'linewidth',2);
xlabel ('Temperature (°C)', 'fontsize', 20);
```

```
ylabel ('Normalized Heat flow W/g_{(NMC811)}', 'fontsize', 20);
ax=gca;
ax.FontSize=30;
ylim ([-1 5]);
xticks(0:50:550);
legend ('MC1 + 1 µL LE', 'MC2 + 1 µL LE', 'MC3 + 1 µL LE');
```

A.2: DSC heat flow of LPSCl shard. Reproduced from [24].

2. Supplementary Figures and Tables

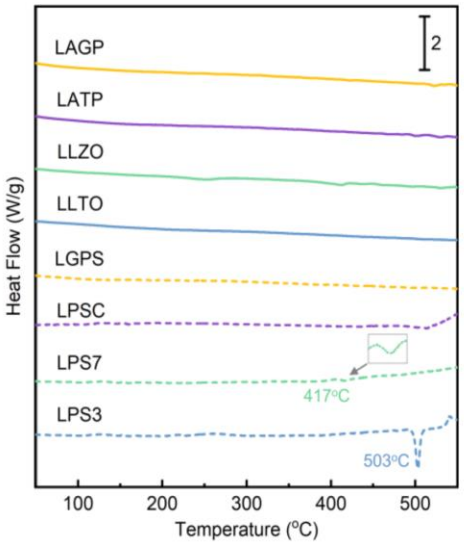

Fig. S1 DSC results of the inorganic SEs.

A.3: DSC heat flow of 1M $LiPF_6$ in EC:DEC (1:1 v/v). Reproduced from Roth *et al.*[25]

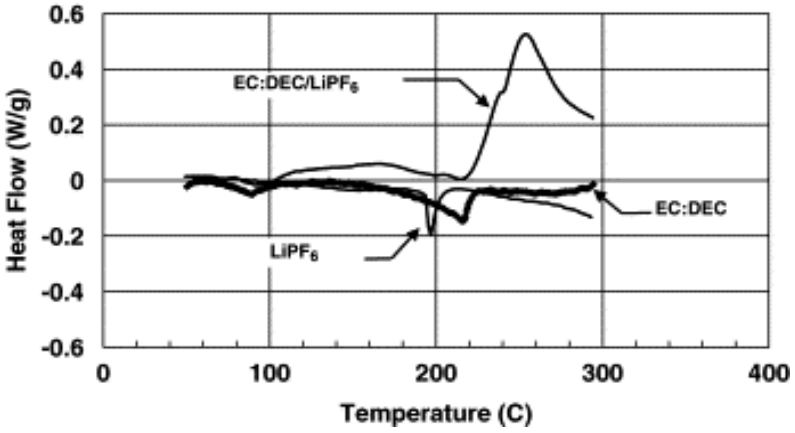

A.4: DSC heat flow of 1M $LiPF_6$ in EC:DEC (1:1 v/v). Reproduced from Wang *et al.*[26]

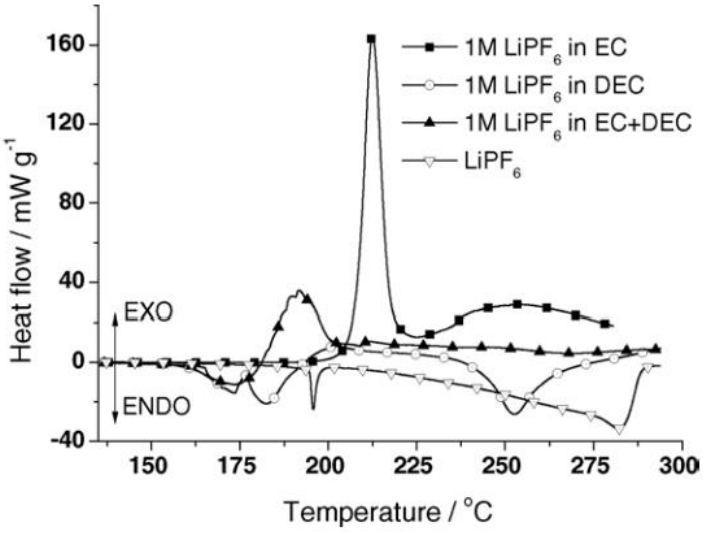

Fig. 2. Heat flow curves of $LiPF_6$, 1 M $LiPF_6$ in EC, DEC, and EC + DEC at 0.2 °C min^{-1} in argon.

A.5: Calculations to determine the maximum volume of liquid electrolyte used in ACE samples.

From the DSC pan specifications, the internal volume is 20 µL (0.02 cm^3) and the maximum operating pressure is 217 bar.

The mass of lithium used is ~ 0.2 mg (0.0002 g), and the density of lithium is 0.534 g / cm^3. Volume of lithium used = Mass of lithium / Density of lithium = 0.0002 g / 0.534 g/ cm^3 = **0.0003745 cm^3.**

The mass of LPSCl used is ~ 11 mg (0.011 g) and its density is 1.64 g cm^{-3}. Therefore, volume of LPSCl used = Mass of LPSCl / Density of LPSCl = 0.011 g / 1.64 g cm^{-3} = **0.0067073 cm^3**.

For the NMC811 used, the diameter is 4 mm (0.4 cm). The area of the NMC811 sheet used is 0.12568 cm^3. The thickness of the current collector is 16 µm and the coating is 63 µm, total thickness is ~ 80 µm (0.008 cm).

Volume = Area × Thickness = 0.12568 cm^3 × 0.008 cm = 0.0010054 cm^3. Since two sheets were used, the total volume of NMC811 used is **0.0020108 cm^3.**

The total volume of the ACE sample in the DSC pan = Volume of lithium + Volume of LPSCl + Volume of NMC811 = 0.009093 cm^3.

The remaining volume = 0.02 cm^3 – 0.009093 cm^3 = **0.010907 cm^3**.

To avoid reaching the maximum operating pressure of the DSC pan considering the oxygen release from NMC811 which reacts with other components to give other gaseous products, a conservative approach is to use 20% of the remaining volume for

the liquid electrolyte. Therefore, the maximum volume of 1M $LiPF_6$ (EC / DEC) that can be added to the DSC pan considering oxygen release and pressure constraint = 0.2 × $V_{remaining}$ = 0.2 × 0.010907 cm^3 = 0.0021814 cm^3 = ~ 2 µL.

Bibliography

1. Kim, T. H.; Park, J. S.; Chang, S. K.; Choi, S.; Ryu, J. H.; Song, H. K., The Current Move of Lithium-Ion Batteries Towards the Next Phase. *Advanced Energy Materials* **2012,** *2* (7), 860-872.

2. Daniel, C.; Mohanty, D.; Li, J.; Wood, D. L. In *Cathode materials review*, 2014; AIP Publishing LLC.

3. Huang, Y.; Li, J., Key Challenges for Grid-Scale Lithium-Ion Battery Energy Storage. *Advanced Energy Materials* **2022,** *12* (48), 2202197.

4. Mauger, A.; Julien, C. M., Critical review on lithium-ion batteries: are they safe? Sustainable? *Ionics* **2017,** *23* (8), 1933-1947.

5. Bates, A. M.; Preger, Y.; Torres-Castro, L.; Harrison, K. L.; Harris, S. J.; Hewson, J., Are solid-state batteries safer than lithium-ion batteries? *Joule* **2022,** *6* (4), 742-755.

6. Märker, K.; Reeves, P. J.; Xu, C.; Griffith, K. J.; Grey, C. P., Evolution of Structure and Lithium Dynamics in $LiNi_{0.8}Mn_{0.1}Co_{0.1}O_2$ (NMC811) Cathodes during Electrochemical Cycling. *Chemistry of Materials* **2019,** *31* (7), 2545-2554.

7. Bak, S.-M.; Hu, E.; Zhou, Y.; Yu, X.; Senanayake, S. D.; Cho, S.-J.; Kim, K.-B.; Chung, K. Y.; Yang, X.-Q.; Nam, K.-W., Structural Changes and Thermal Stability of Charged $LiNi_xMn_yCo_zO_2$ Cathode Materials Studied by Combined In Situ

Time-Resolved XRD and Mass Spectroscopy. *ACS Applied Materials & Interfaces* **2014,** *6* (24), 22594-22601.

8. Noh, H.-J.; Youn, S.; Yoon, C. S.; Sun, Y.-K., Comparison of the structural and electrochemical properties of layered $Li[Ni_xCo_yMn_z]O_2$ (x = 1/3, 0.5, 0.6, 0.7, 0.8 and 0.85) cathode material for lithium-ion batteries. *Journal of Power Sources* **2013,** *233*, 121-130.

9. Shadike, Z.; Chen, Y.; Hu, E.; Zhang, J.; Yang, X.-Q., Interphasial engineering for Ni-rich NMC cathode materials. *Trends in Chemistry* **2023,** *5* (10), 775-787.

10. Akhilash, M.; Salini, P. S.; John, B.; Supriya, N.; Sujatha, S.; Mercy, T. D., Thermal stability as well as electrochemical performance of Li-rich and Ni-rich cathode materials—a comparative study. *Ionics* **2023,** *29* (3), 983-992.

11. Yu, C.; Zhao, F.; Luo, J.; Zhang, L.; Sun, X., Recent development of lithium argyrodite solid-state electrolytes for solid-state batteries: Synthesis, structure, stability and dynamics. *Nano Energy* **2021,** *83*, 105858.

12. Chen, Y.-T.; Marple, M. A. T.; Tan, D. H. S.; Ham, S.-Y.; Sayahpour, B.; Li, W.-K.; Yang, H.; Lee, J. B.; Hah, H. J.; Wu, E. A.; Doux, J.-M.; Jang, J.; Ridley, P.; Cronk, A.; Deysher, G.; Chen, Z.; Meng, Y. S., Investigating dry room compatibility of sulfide solid-state electrolytes for scalable manufacturing. *Journal of Materials Chemistry A* **2022,** *10* (13), 7155-7164.

13. Zhou, L.; Minafra, N.; Zeier, W. G.; Nazar, L. F., Innovative Approaches to Li-Argyrodite Solid Electrolytes for All-Solid-State Lithium Batteries. *Accounts of Chemical Research* **2021,** *54* (12), 2717-2728.

14. Bai, X.; Duan, Y.; Zhuang, W.; Yang, R.; Wang, J., Research progress in Li-argyrodite-based solid-state electrolytes. *Journal of Materials Chemistry A* **2020,** *8* (48), 25663-25686.

15. Roy, K.; Banerjee, A.; Ogale, S., Search for New Anode Materials for High Performance Li-Ion Batteries. *ACS Applied Materials & Interfaces* **2022,** *14* (18), 20326-20348.

16. Lin, D.; Liu, Y.; Cui, Y., Reviving the lithium metal anode for high-energy batteries. *Nature Nanotechnology* **2017,** *12* (3), 194-206.

17. Cheng, X.-B.; Zhao, C.-Z.; Yao, Y.-X.; Liu, H.; Zhang, Q., Recent Advances in Energy Chemistry between Solid-State Electrolyte and Safe Lithium-Metal Anodes. *Chem* **2019,** *5* (1), 74-96.

18. Liang, B.; Liu, Y.; Xu, Y., Silicon-based materials as high-capacity anodes for next generation lithium ion batteries. *Journal of Power Sources* **2014,** *267*, 469-490.

19. Ko, M.; Chae, S.; Cho, J., Challenges in Accommodating Volume Change of Si Anodes for Li-Ion Batteries. *ChemElectroChem* **2015,** *2* (11), 1645-1651.

20. Shi, J.; Jiang, K.; Fan, Y.; Zhao, L.; Cheng, Z.; Yu, P.; Peng, J.; Wan, M., Advancing Metallic Lithium Anodes: A Review of Interface Design, Electrolyte Innovation, and Performance Enhancement Strategies. *Molecules* **2024,** *29* (15), 3624.

21. Cooper, A.; Johnson, C. M., Differential Scanning Calorimetry. Humana Press: pp 125-136.

22. Steinmann, W.; Walter, S.; Beckers, M.; Seide, G.; Gries, T., Thermal Analysis of Phase Transitions and Crystallization in Polymeric Fibers. In *Applications of Calorimetry in a Wide Context*, Amal Ali, E., Ed. IntechOpen: Rijeka, 2013; p Ch. 12.

23. Yang, S.-J.; Hu, J.-K.; Jiang, F.-N.; Cheng, X.-B.; Sun, S.; Hsu, H.-J.; Ren, D.; Zhao, C.-Z.; Yuan, H.; Ouyang, M.; Fan, L.-Z.; Huang, J.-Q.; Zhang, Q., Oxygen-induced thermal runaway mechanisms of Ah-level solid-state lithium metal pouch cells. *eTransportation* **2023,** *18*, 100279.

24. Rui, X.; Ren, D.; Liu, X.; Wang, X.; Wang, K.; Lu, Y.; Li, L.; Wang, P.; Zhu, G.; Mao, Y.; Feng, X.; Lu, L.; Wang, H.; Ouyang, M., Distinct thermal runaway mechanisms of sulfide-based all-solid-state batteries. *Energy & Environ. Sci.* **2023,** (16), 3552-3563.

25. Roth, E. P.; Doughty, D. H.; Franklin, J., DSC investigation of exothermic reactions occurring at elevated temperatures in lithium-ion anodes containing PVDF-based binders. *Journal of Power Sources* **2004,** *134* (2), 222-234.

26. Wang, Q.; Sun, J.; Yao, X.; Chen, C., Thermal stability of $LiPF_6$/EC+DEC electrolyte with charged electrodes for lithium ion batteries. *Thermochimica Acta* **2005,** *437* (1), 12-16.